Cement and Concrete Composites 153 (2024) 105693

Contents lists available at ScienceDirect

Cement and Concrete Composites

journal homepage: www.elsevier.com/locate/cemconcomp

Reducing carbonation degradation and enabling CO_2 sequestration in alkali-activated slag using cellulose nanofibers

Nithya Nair, Warda Ashraf [*]

Department of Civil Engineering, University of Texas at Arlington, Nedderman Hall, 416 Yates St., Arlington, TX, 76010, USA

ARTICLE INFO

Keywords:
Cellulose nanofibers
Alkali-activated slag
Carbonation
CO_2 sequestration

ABSTRACT

This study evaluated the role of cellulose nanofibers (CNF) in reducing the carbonation degradation of alkali-activated slag (AAS) samples. AAS samples prepared with different dosages of CNF (0 %, 0.10 %, and 0.80 % by weight of the binder) were exposed to natural and accelerated carbonation for up to 90 days. The effects of carbonation on the microstructure of AAS paste samples were monitored using FTIR, XRD, TGA, MIP, and BSE/SEM. It was observed that after 90 days of natural carbonation, the control batch exhibited a reduction in compressive strength, whereas the CNF batches showed an enhancement. Notably, the CNF-containing batches maintained consistent strength over time, with no reduction in strength. Similarly, after 90 days of accelerated carbonation, CNF 0.10 % and CNF 0.80 % showed an increase in compressive strength compared to the control batch. Despite this enhancement in compressive strength, microstructural studies indicated that the addition of CNF increased the extent of carbonation, leading to a higher amount of $CaCO_3$ formation and C–S–H/C-A-S-H decalcification compared to the control batch. The beneficial effects of CNF on the strength despite increased C–A–S–H decalcification are attributed to their reinforcing effects and the ability to form composites with $CaCO_3$.

1. Introduction

Alkali-activated materials (AAM) have a lower carbon footprint than Ordinary portland cement (OPC) concrete, which accounts for approximately 6%–8% of global anthropogenic CO_2 emissions [1,2]. The life cycle assessment (LCA) of the production of OPC concrete and alkali-activated concrete showed that the ground granulated blast furnace slag (GGBFS) based AAM concrete has 57 % lower global warming potential (GWP) than OPC concrete [2]. Numerous studies have reported the benefits associated with the utilization of alkali-activated slag (AAS) cement, emphasizing its advantages, such as rapid strength development, enhanced durability, and resistance to fire and chemical degradation [3–7]. While GGBFS-based AAM concrete has lower CO_{2eq} emissions than OPC concrete, its poor resistance to carbonation hinders widespread acceptance in construction practices. Carbonation is an irreversible and unavoidable reaction resulting from the presence of CO_2 in our atmosphere. Carbonic acid is formed when CO_2 diffuses through concrete pores and reacts with the pore solution. As a result, the formation of carbonic acid lowers the pH and, thereby, the alkalinity of the cementitious system. The reduction in alkalinity leads to depassivation of the reinforcement surface and eventually can lead to reinforcement corrosion [8–10]. However, if carbonation-induced performance degradation is prevented, such reaction will allow additional CO_2 sequestration in AAS, and therefore, further reduce their carbon footprint [11].

The process of carbonation in the AAM system is more complex than in the OPC system. In the AAM system, the absence of portlandite (CH) results in the direct decalcification of the primary hydration product, C–S–H/C-A-S-H. This transformation leads to the formation of highly polymerized silica gel [12–19]. As the carbonation process progresses, it causes the formation of different types of $CaCO_3$ polymorphs following Ostwald's process. These polymorphs include metastable amorphous calcium carbonate (ACC), vaterite, aragonite, and finally, stable crystalline calcite [19–22]. As a result of the decalcification of C–S–H/C-A-S-H and the subsequent formation of calcite increase the porosity of the matrix, leading to carbonation shrinkage, lower compressive strength, and diffusion of harmful ions such as chlorides and sulfates into concrete [6,23,24]. Controlling the primary polymorph of $CaCO_3$ is a promising approach to reducing the carbonation in the AAM system. Studies have shown that increasing magnesium content in slag pastes delays the decalcification of C-A-S-H gel hydrate by forming stable Mg-based amorphous calcium carbonate [25,26]. Other additives

---

[*] Corresponding author.
E-mail address: warda.ashraf@uta.edu (W. Ashraf).

https://doi.org/10.1016/j.cemconcomp.2024.105693
Received 7 April 2024; Received in revised form 16 July 2024; Accepted 3 August 2024
Available online 5 August 2024
0958-9465/© 2024 Elsevier Ltd. All rights are reserved, including those for text and data mining, AI training, and similar technologies.

like $Ca(OH)_2$, $Zn(OH)_2$, air-entraining agents, and shrinkage-reducing admixtures can also stabilize amorphous $CaCO_3$ polymorphs and control carbonation in AAS systems [27]. A study by Ke et al. investigated the use of sodium carbonate as an activator, resulting in a sustained mechanical performance in contrast to sodium silicate-activated slag cement during carbonation [11].

Inspired by those previous studies, this work explored the effectiveness of CNF in reducing the carbonation-induced deterioration of AAM. Cellulose-based nanomaterials derived from plants can be a cost-effective and environmentally friendly additive for cementitious composites [28]. Incorporating CNF into a cementitious matrix has yielded significant improvements, such as the reduction in plastic shrinkage [29,30], mechanical properties, including compressive strength, flexural strength, and fracture toughness [31–35], as well as enhanced long-term durability [36]. In contrast to conventional reinforcement bars, CNF exhibit distinctive characteristics by not only providing crack-bridging effects due to their high aspect ratio [37,38] but also influencing the hydration and microstructural properties of the cementitious system [31,32,35]. Cao et al. reported that nanocellulose slows early-stage cement hydration and enhances later-stage hydration through steric stabilization and short-circuit diffusion effect [39]. Low CNF dosage was also observed to enhance the long-term durability against sulfate attack, as evidenced by improved resistance of cement mortar after six months of exposure [36]. Overall, CNF emerges as a promising additive for high-performance cementitious composites. However, limited studies have been conducted using CNF to reduce carbonation deterioration. Zhang et al. examined the microstructure and moisture transport in OPC pastes, both with and without CNF, under non-carbonated and accelerated carbonation conditions, with 4 % CO_2 concentration and 57 % relative humidity [40]. The findings revealed that the inclusion of CNFs caused the development of drying cracks and did not exhibit favorable effects, as CNFs were found to hinder cement hydration, coarsen the microstructure, and increase both moisture transport and porosity [40]. On the other hand, the presence of CNFs resists carbonation by creating fewer large capillary pores than materials without CNF. Microstructure studies confirmed this finding that the amount of carbonated C–S–H and ettringite is halved when compared to the batch without CNF [40]. Additionally, a study by Khan et al. [41] indicated that the addition of CNF enhances the performance of carbonated cementitious composites.

Limited research has been conducted on the role of CNF in the AAS system. Ez-Zaki et al. studied the influence of surface-functionalized CNFs on rheology, microstructure and strength of alkali-activated in comparison to their effects on OPC [42]. The research demonstrated that CNFs have the potential to act as water reservoirs, preventing segregation and bleeding. However, CNFs also increase the volume of air voids and create porous agglomerates due to the swelling ability of nanofibrils. This effect is less significant in Ground granulated blast furnace slag (GGBFS) compared to the OPC system. The study concluded that the effect of CNFs on GGBFS pastes is complex and necessitates further research to evaluate their impact on the dimensional stability of hardened specimens [42].

Considering the crack-bridging effects of CNF, we hypothesize that the addition of CNF in AAS can reduce the carbonation induced damage in such systems. The aim of this study is to verify the hypothesis by providing fundamental understanding of the effects of CNF in alkali-activated slag subjected to natural and accelerated carbonation. The present study is designed to achieve a set of specific research objectives: (i) to understand the effect of CNF on alkali-activated slag system, (ii) to evaluate the mechanical performance of the AAS with CNF under carbonation conditions, (iii) to comprehensively examine microstructural changes, with an emphasis on alterations in silicate and carbonate phases during carbonation of AAS samples, using CNF.

2. Materials and sample preparation

2.1. Materials

A commercially available slag (Grade 120) supplied by Cemex, USA, was used for the study. Table 1 below provides the oxide composition of the slag, determined by X-Ray Fluorescence spectroscopy (XRF) (Rigaku NEXCG). The alkali-activator used was industrial grade (high purity of 99 ± 1 %) sodium hydroxide (NaOH) in pellet form. The fine aggregate used was standard sand, as per ASTM C778. Samples of delignified-CNF were provided by Performance Biofilaments, Inc. (Canada). Table 2 presents the characteristics of CNF. The CNF had a thick, slurry-like consistency, with a solid content of 34 % in water. To maintain the water to binder ratio, the total amount of water required was adjusted by subtracting the amount of free water present in the CNF.

2.2. Sample preparation

To understand the effect of the addition of CNFs on alkali-activated slag in terms of compressive strength and microstructure, paste and mortar samples were prepared for all the batches. The slag was activated by mixing with the sodium hydroxide solution at a water-to-binder ratio of 0.45 and constant Na_2O of 7 % by weight of the slag. The activator solution was prepared 24 h prior to the preparation of paste samples in order to cool down to room temperature. The activator solution was then mixed with CNFs using a high-shear blender for 3 min as per the supplier's recommendation. The CNFs were added at 0.10 % and 0.80 % by weight of the slag. The samples were prepared using a Hobart mixer. After casting, the paste samples were kept at room temperature of 25 ± 2 °C and higher relative humidity of 95 % for 24 h. The demolded samples were kept in an environment at a temperature of 25 ± 2 °C and relative humidity of 95 ± 2 %. The humidity was controlled by salt solution. For the preparation of the mortar samples, the water-to-binder ratio was the same as that of the paste samples, and the sand-to-binder ratio was maintained at 3:1. The mortar samples were cast into 50 mm cube molds for compressive strength measurements. Paste samples were prepared in a rectangular mold of 5 cm × 1 cm × 1 cm for microstructural investigations.

The influence of CNF on alkali-activated slag samples were investigated under (i) natural and (ii) accelerated carbonation conditions. (i) For the natural carbonation study, the compressive strength of mortar samples was tested at 7, 28, and 90 days of curing at a temperature of 25 ± 2 °C and relative humidity of 95 ± 2 %. (ii) For accelerated carbonation, after 28 days of curing (temperature of 25 ± 2 °C and relative humidity of 95 ± 2 %), both the pastes and mortar samples were dried for three days in a vacuum to remove the moisture content prior to accelerated carbonation. After drying, the samples were kept inside the carbonation chamber. The accelerated carbonation was conducted at 25 °C, relative humidity of 65 % and 20 % CO_2 concentration. The carbonated mortar and paste samples were tested over the same duration as those exposed to natural carbonation.

For microstructural analysis, the paste samples were sealed on all sides, except one side was exposed to simulate unidirectional CO_2 diffusion (Fig. 1). During the testing period, the paste sample was divided into five equal parts. Two sections, the exposed section (SEC 1) and mid-section (SEC 3), were taken for microstructural analysis. Paste samples were collected at intervals corresponding to those used for mortar samples, and further reactions were halted using vacuum treatment with isopropanol.

Table 1
Chemical composition of slag.

(wt. %)	CaO	SiO_2	Al_2O_3	Fe_2O_3	SO_3	MgO	K_2O	Na_2O
Slag	36.4	29.6	15.6	0.372	5.19	9.69	0.305	0.762

Table 2
Properties of cellulose nanofibers.

Properties of cellulose nanofibers	
Diameter of Fibril	80–300 nm
Length of Fibril	100–500 μm
Aspect ratio	800–1000 L/D
Density	2.5 g/cm^3
Surface Area	80,000 m^2/kg

2.3. Test procedures

The TAM Air isothermal calorimeter by TA Instruments was used to measure the heat of hydration. Paste samples were placed into the calorimeter chamber immediately after mixing, and signal corrections were applied 45 min later. The measurement of heat of hydration extended up to 190 h at a temperature of 23 °C. The tests were repeated for multiple batches, and the standard deviation of total heat measurements consistently remained below 2 %. The compressive strength of 50 mm mortar cubes was measured following the ASTM C109. The compressive strength was measured after exposure to natural and accelerated carbonation for 7, 28, and 90 days. The Fourier-Transformed Infrared Spectroscopy (FTIR) spectra of the powdered samples were collected using the Nicolet iS5 in Attenuated Total Reflection (ATR) mode. The frequency range was 400–4000 cm^{-1}, with a 4 cm^{-1} resolution and 32 scans per sample. The signal-to-noise ratio was lower than 3:1. The powdered samples were tested at 7, 28 and 90 days of natural and accelerated carbonation exposure.

A commercially available TGA 550 TA instrument was used for thermogravimetric analysis (TGA). Paste samples were collected after exposure to natural and accelerated carbonation for 7, 28, and 90 days. After grinding paste samples using a mortar and pestle, approximately 30–40 mg of the samples were loaded into a platinum pan and kept under isothermal conditions at around 25 °C for 3 min. N_2 gas was purged into the chamber to ensure an inert environment. The temperature was ramped up to 980 °C, with a heating rate of 15 °C per minute. Initially, three TGA tests were done for three replicate samples, and the standard deviation of the results was less than 2 %. Consequently, the TGA test was performed with only one sample for the remaining batches.

X-ray Diffraction (XRD) analysis of the powdered samples was done on a Bruker D-8 spectrometer, using Cu Kα radiation (40 kV, 40 mA). The diffraction patterns were obtained for the range of 5° - 60° (2θ), using a step size of 0.03 per second and a scanning speed of 1 s per step.

The change in the porosity of the microstructure due to natural and accelerated carbonation is assessed using mercury intrusion porosimetry (MIP). The porosity was measured using the Autopore IV 9500 v2.03.01 by Micromeritics Instrument Corporation at a pressure of 413 MPa. To reduce the uncertainty or error percentage in the test, the sample mass was kept consistent for all the batches.

The Backscattered Electrons Imaging (BSE) and Secondary Electron Microscopy images of paste samples were captured using the Hitachi 3000 N SEM. The hydration of samples was first stopped with isopropanol, followed by vacuum-drying. Later, the samples were impregnated with epoxy resin and polished. For BSE/SEM imaging, the polished samples were coated with Gold (Au) and Platinum (Pt). The instrument operated in high vacuum mode with an accelerated voltage of 25-kV and a working distance of 15 mm. Additionally, energy-dispersive X-ray (EDS) points were also taken.

3. Results and discussions

3.1. Effect of CNF on alkali activation

3.1.1. Heat of hydration

Fig. 2 illustrates the heat of hydration of alkali-activated slag (AAS) paste samples at different dosages of CNF for seven days. Analyzing the heat flow per gram of binder (Fig. 2 a), a high-intensity heat flow peak was exhibited by the CNF batches, particularly at 0.10 % dosage compared to the control and 0.80 % batch. This indicates that the CNF accelerated the hydration of AAS binders. Notably, at the end of seven days, both dosages of CNFs exhibited higher total heat compared to the control batch (Fig. 2 b). This improved reaction of AAS due to the addition of CNF can be attributed to the higher surface area of CNF, which induces the nucleation effect, leading to an acceleration in slag hydration [36].

3.2. Effect of CNF on natural carbonation of alkali-activated slag

3.2.1. Macroscale effects

Fig. 3 shows the compressive strength of mortar samples, without the addition of CNF and with CNF, at two different dosages (0.10 % and 0.80 %), tested at 7, 28, and 90 days of exposure conditions. After 7 days, the control batch (without CNF) showed a slightly higher compressive strength (22.7 MPa) when compared to the 0.10 % CNF dosage (21.2 MPa). However, a higher dosage of CNFs resulted in a reduction of compressive strength (19.4 MPa). The decreased compressive strengths observed at a higher dosage (0.80 %) is attributed to the agglomeration of fibers, creating weak zones in the matrix [36]. It is difficult to establish a direct correlation between the heat of hydration and early-age compressive strength (7 days). The initial retardation in the rate of hardening can be attributed to the affinity of negative carboxyl and hydroxyl groups in the CNF for positively charged alkali ions (Na^+) [36]. After 28 days, the compressive strength of all batches increased. The batch with 0.10 % CNF exhibited higher compressive strength (31.1 MPa) than the control (29.5 MPa) and 0.80 % batches (25.8 MPa).

After 90 days, the natural carbonation process starts to significantly affect the strength of the mortar samples. Compared to their 28-day compressive strength, the control batch experienced a decrease (27.2 MPa), while the batches with CNF 0.10 % (31.7 MPa) and 0.80 % (25.2 MPa) showed a slight improvement in compressive strength. These batches maintained consistent strength as the specimens aged and did not experience a drop in strength.

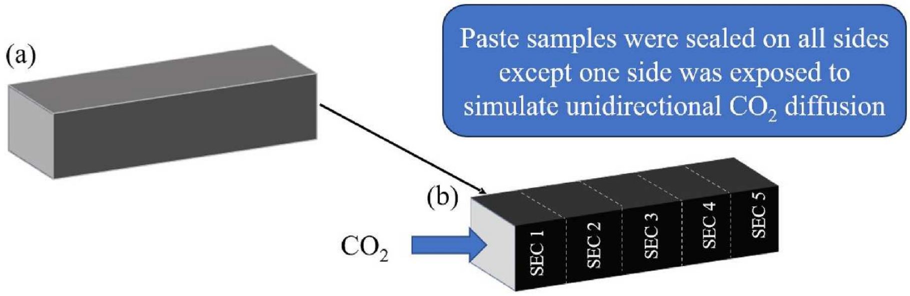

Fig. 1. Schematic diagram showing (a) AAS paste sample (5 cm × 1 cm × 1 cm) and (b) AAS paste sample sealed on all sides except for one side with marked sections.

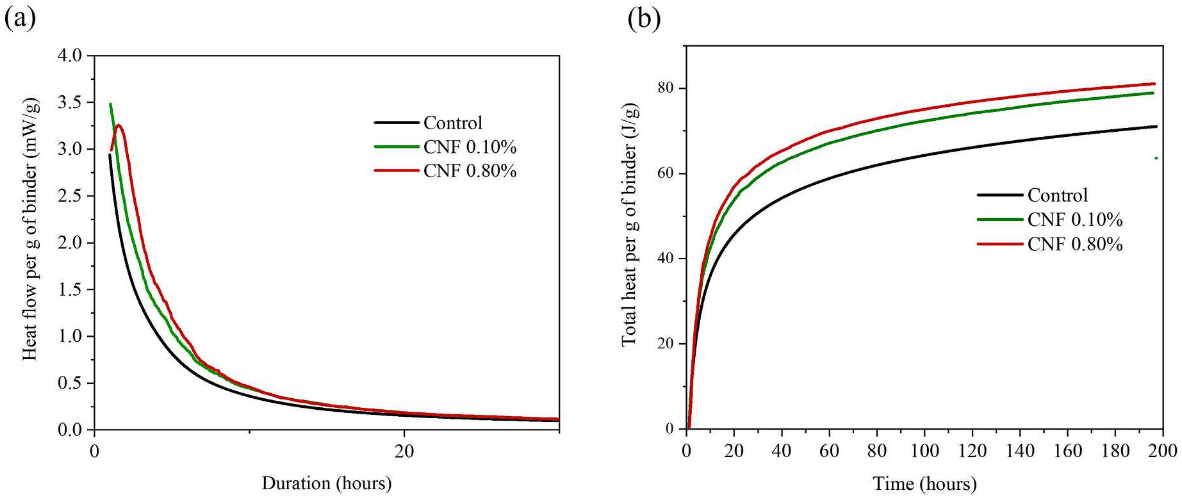

Fig. 2. Isothermal calorimeter measurement of alkali-activated slag containing CNF (a) Heat flow measurement, (b) Total heat per g of binder.

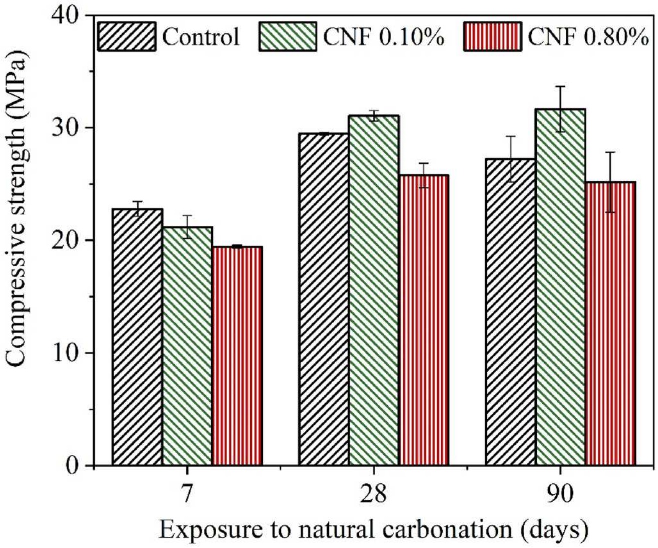

Fig. 3. Compressive strengths of control, CNF 0.10 %, and CNF 0.80 % batches after 7, 28, and 90 days of natural carbonation.

3.2.2. Microscale effects

3.2.2.1. Silicate and carbonate phase alteration due to natural carbonation. Fig. 4 shows the FTIR spectra of (a) control, (b) CNF 0.10 % and (c) CNF 0.80 % at 7, 28, and 90 days of natural carbonation. In this study, the FTIR peak range from 800 cm^{-1} to 1800 cm^{-1} was used to qualitatively compare the effects of CNF in AAS subjected to natural carbonation. The FTIR spectra can be divided into three main groups associated with: (i) Si–O bond vibrations, (ii) H–OH bond vibrations, and (iii) CO_3^{2-} bond vibrations. The wide FTIR absorption band between 800 cm^{-1} and 1200 cm^{-1} corresponds to the asymmetric stretching vibration (v_3) of the Si–O bond, and the peak location varies based on the Ca/Si ratio [20,43,44]. The peaks at 940 - 980 cm^{-1} due to the asymmetrical stretching vibration (v_3) of the Si–O bond of the Q^2 tetrahedron correspond to the calcium alumino-silicate hydrate gel or calcium silicate hydrate gel (C-A-S-H/C–S–H) [45,46]. The peaks between 1050 and 1080 cm^{-1} and 1120 - 1200 cm^{-1} indicate the highly polymerized silicate of Q^3 and Q^4 tetrahedron units, respectively [45,46].

The bending vibration of the H–OH group within the reaction products can be observed in the 1645 cm^{-1} FTIR peak band [22]. The $CaCO_3$ polymorphs appear in three distinct regions such as (i) 1300–1500 cm^{-1} due to asymmetrical stretching vibration (v_3), (ii) 800–900 cm^{-1} due to out-of-plane bending (v_2), and (iii) 700–750 cm^{-1} due to in-plane bending (v_4); of the CO_3^{2-} bond [21,43,44]. Additionally, the sharp peaks at 872 cm^{-1} and 711 cm^{-1} were attributed to the characteristic calcite peaks [20,21,43,47]. The metastable $CaCO_3$ polymorph, such as ACC as well as vaterite, can be identified at a split peak at around 1350 cm^{-1} and 1390 cm^{-1}, respectively, due to the asymmetrical stretching vibration (v_3) of the O–C–O bonds of CO_3^{2-} group [44,48].

In the control batch (Fig. 4 a), the 940 cm^{-1} peak corresponding to the Si–O bond in the main hydration product, C-A-S-H gel (Q^2), was evident at 7 days. As the curing period extends, the intensity of the Q^2 peak increases, indicating enhanced hydration, which can be observed at 28 days. Simultaneously, due to silica gel polymerization, additional peaks at 1018 cm^{-1} and 1118 cm^{-1}, which indicate the presence of Q^3 and Q^4 units, respectively, can be observed. Regarding the formation of $CaCO_3$ polymorph, the peak shifts at early ages (7 and 28 days) to 1372 cm^{-1}, indicating the presence of ACC or vaterite, and the small peak of 1414 cm^{-1} indicates calcite formation. After 90 days, there was a slight shift in the Q^2 peak, with reduced peak intensity at 940 cm^{-1} to a higher wave number and a substantial increase in the peak observed at 1414 cm^{-1}, with a shoulder peak at 1475 cm^{-1} indicating the formation of Trona [22,49]. This indicates that there is a high degree of polymerization occurring from Q^2 to Q^3 and Q^4 units due to the decalcification of the C-A-S-H gel that has undergone carbonation. Additionally, the presence of water in hydration products can be seen by the H–OH bond at 1645 cm^{-1}. This peak decreases with time, indicating the initiation of carbonation-induced drying of the hydration products.

In the CNF 0.10 % batch (Fig. 4 b), there is an observed increase in peak intensity at 940 cm^{-1} compared to the control batch after 28 days of curing. This rise can be attributed to the accelerated hydration facilitated by the addition of CNF. While CNF initially delays hydration, it later expedites the process by providing additional nucleation sites. The improved mechanical strength of the alkali-activated binder is particularly evident at advanced curing stages. Similar to the control batch, the CNF 0.10 % batch exhibits additional peaks at 1024 cm^{-1} and 1123 cm^{-1}, indicating the presence of Q^3 and Q^4 units, respectively, due to a higher degree of silica polymerization.

After three months of natural carbonation, the peak intensity at 940 cm^{-1} was reduced, but no peak shift was observed in the CNF 0.10 % batch as compared with the control batch. Nevertheless, the appearance of a small peak at 1475 cm^{-1} and a peak band centered at 1414 cm^{-1} indicates the presence of $CaCO_3$ polymorphs resulting from the decalcification of C-A-S-H gel. However, the extent of decalcification was

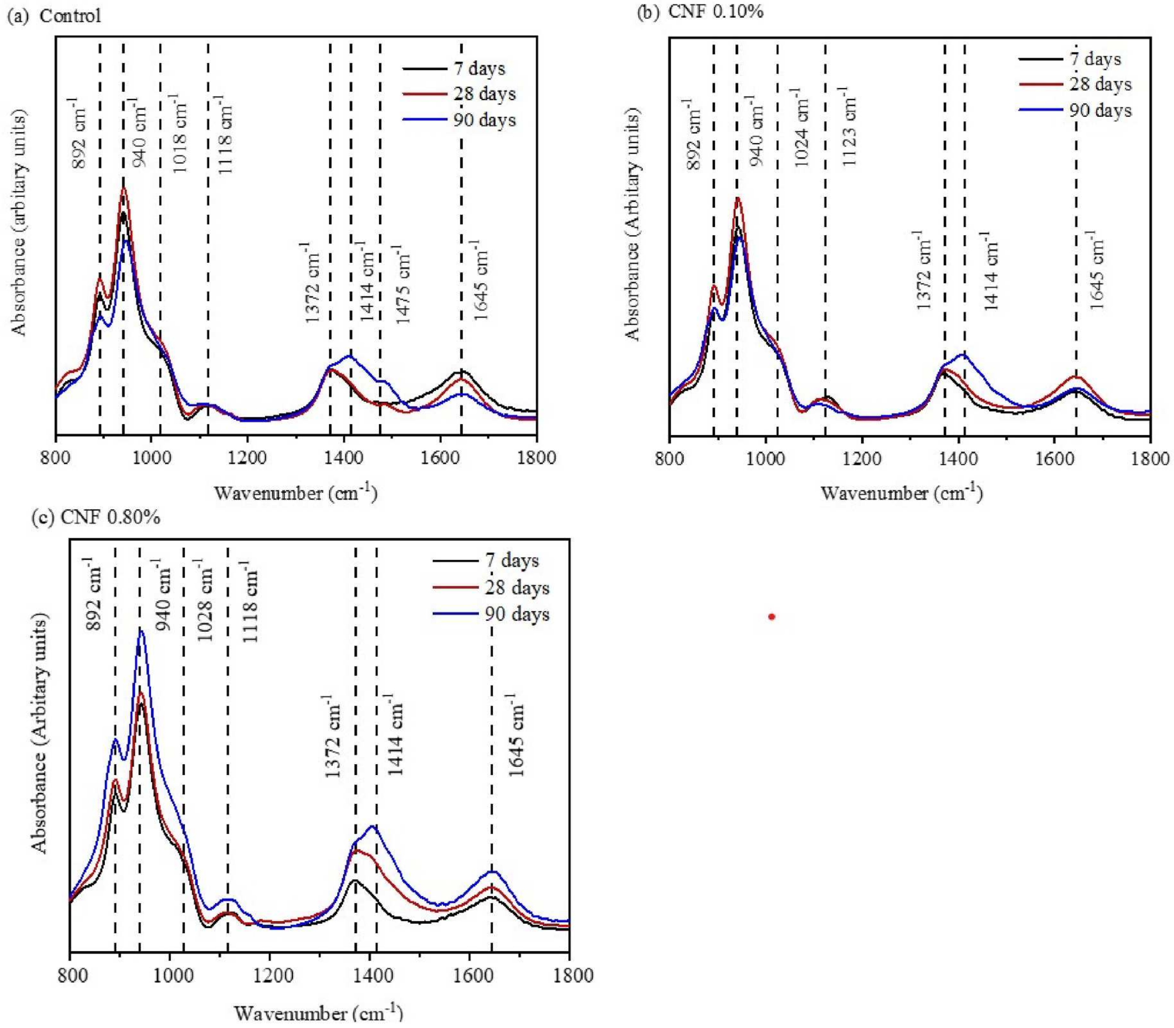

Fig. 4. FTIR spectra of (a)control, (b) CNF 0.10 % and (c) CNF 0.80 % batches after 7, 28, and 90 days of natural carbonation.

notably less in the alkali-activated slag system, with CNF 0.10 % batch. This can be because CNF contributes to the additional C-A-S-H formation and binding $CaCO_3$ polymorphs, leading to a refined pore structure and a densified microstructure. This phenomenon elucidates the relatively minimal compressive strength loss in the CNF-incorporated batch compared to the control batch.

The CNF 0.80 % (Fig. 4 c) mechanism differs from the trend of control and CNF 0.10 % batches. With an increase in the duration of curing age, even after three months, the peak intensity at 940 cm^{-1} increases. The peak intensity of calcite at 1414 cm^{-1} also increases with the curing age. This observation was confirmed by the increase in the 1645 cm^{-1} peak due to the H–OH bond indicating the vibration of water molecules within the reaction products. While, as previously mentioned, CNF contributes to additional nucleation sites for C-A-S-H growth, the agglomeration-induced pores also play a role. This contributes to an increase in the decalcification of C-A-S-H gel, facilitated by the ingress of CO_2 gas through the pores. This hypothesis is consistent with the compressive strength findings.

Fig. 5 presents the TGA plot of the control, CNF 0.10 %, and CNF 0.80 % batches at 7, 28, and 90 days of natural carbonation. Before carbonation, significant weight loss was noted at temperatures below 600 °C and was attributed to the decomposition of hydration products [21,45]. The loss of weight below 600 °C was caused by the evaporation of loosely bound water and dehydration of the primary hydration product, such as C-A-S-H gel, AFt, and hydrotalcite [24,50,51]. The majority of literature identifies the loss of free water surrounding the C-A-S-H gel and the interlayer water within C-A-S-H, which was released when the temperature is below 250 °C [22,52]. Another hydration product, particularly in NaOH-activated slag, is hydrotalcite. Hydrotalcite (Ht) is Mg–Al double hydroxide layers, which act as CO_2 absorbent into the interlayers [50,53]. The decomposition temperature range of hydrotalcite exists in a broader temperature range. According to research by Bernal et al., the decomposition temperature of hydrotalcite was found to be 170 °C [18]. However, the study conducted by Park et al. revealed a significantly higher decomposition temperature of 400 °C [54]. It has been found that pure CNFs undergo thermal decomposition at approximately 360 °C [55]. When subjected to carbonation, AAS samples undergo irreversible decalcification caused by the reaction between diffused CO_2 and C-A-S-H gel formation of aluminosilicate hydrate type gel and various polymorphs of $CaCO_3$ [12,13]. The temperature range of 200–800 °C is the decomposition range of the $CaCO_3$ polymorphs [21,45]. The gradual weight loss in this temperature range was due to the decomposition of $CaCO_3$ polymorphs, such as ACC, vaterite, and aragonite, in order of their thermal stability [20,21,43]. The most stable form of $CaCO_3$, calcite, undergoes a sharp weight loss between 600 and 800 °C [21,45].

For the control batch (Fig. 5 a), it was observed that as the specimen ages, the weight loss intensity peak between 20 and 200 °C, which was caused by the decomposition of C–S–H/C-A-S-H gel, reduces. After 7 days, the C-A-S-H peak gradually increased up to 28 days of curing due to enhanced hydration. Furthermore, in addition to the C-A-S-H gel, hydrotalcite was observed in all batches of NaOH-activated slag with a

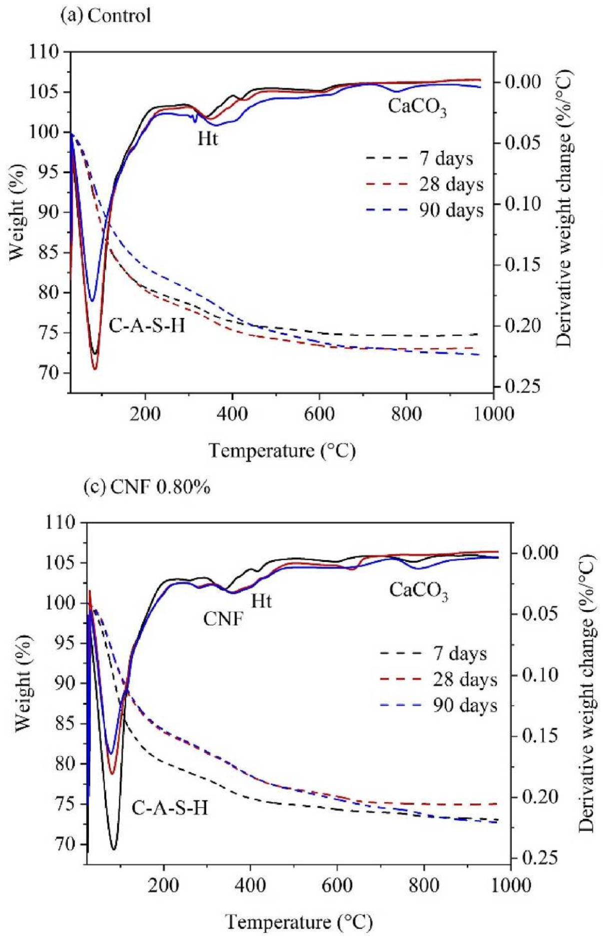

Fig. 5. TGA plot of (a) control (b) CNF 0.10 % (c) CNF 0.80 % batches after 7, 28, and 90 days of natural carbonation.

weight loss temperature ranging between 300 and 400 °C. After 3 months of natural carbonation, the C-A-S-H gel undergoes decalcification, which causes a shift towards a lower temperature range when compared to uncarbonated samples. In a previous study by Bernal (2016), it was reported that the weight loss band shifts to a lower temperature range due to the decalcification of the C-(N)-A-S-H gel. This shift occurs at 52 °C and is identified as a result of the water in the carbonated gel being more loosely bound than the original C-(N)-A-S-H gel [22]. As mentioned in the previous section, carbonation leads to the decalcification process, causing the disintegration of the C-A-S-H gel into alumina-silica gel and $CaCO_3$ polymorphs. The weight loss caused by the decomposition of amorphous $CaCO_3$, and calcite decomposition can be seen at temperatures of 600–700 °C and 750–850 °C, respectively, and it increases with the age of the specimen. This results in a loss of cohesion and successive loss of compressive strength with increasing age of exposure.

It was observed that for CNF 0.10 %, the weight loss intensity peak between 20 and 200 °C was almost the same at 7 and 28 days; however, it reduced after 90 days (Fig. 5 b). The results also showed an increase in weight loss within temperatures of 600–700 °C and 750–850 °C as the specimens aged, indicating the formation of $CaCO_3$ polymorphs due to the decalcification of C-A-S-H gel. In the case of the CNF 0.80 % batch, a broader peak intensity of approximately 100 °C was observed after 7 days of curing (Fig. 5 c). This may be because of the free water entrained by the CNFs, causing a delay in the initial hydration due to the alkali binding of CNF. The CNF 0.80 % batch also showed a consistent reduction during the increase in curing days with the shift of the C-A-S-H peak to the lower temperature band due to decalcification, as mentioned previously, for the other two batches. Therefore, higher dosages of CNFs caused the fibers to agglomerate, which prevented additional nucleation sites for C-A-S-H gel formation. This increased porosity may have accelerated the carbonation over time compared to the control batch and CNF 0.10 % batch.

Fig. 6 shows the XRD pattern of the control, CNF 0.10 %, and CNF 0.80 % batches after 7, 28, and 90 days of natural carbonation. As previously discussed, C-A-S-H and hydrotalcite-type phases are the main hydration products of alkali-activated slag (AAS), regardless of the activator used. However, the structure of C–S–H varies according to the type of activator used. In the case of NaOH-activated slag systems, the C–S–H gels are more crystalline and contain less bound water [56]. Most of the studies have reported the formation of zeolites such as natrolite, gismondine, pirssonite, and other alkali cations containing crystalline phases with age of the AAS samples. However, no such zeolites were traceable from the XRD analyses presented in this study. Wang and Scrivener [50] made similar observations in their research on the microstructural development of NaOH and water glass-activated slag pastes at room temperature after wet curing at 20 °C up to 15 months or at 80 °C for 14 days. The reason was stated that from the X-ray microanalysis, the alkali ions species, especially Na^+ ions, present in significant quantities in the solution during specimen preparation, can dissolve and precipitate out on the surface of hydration products [50]. The SEM/BSE observations in this study (discussed in detail in this section) showed the presence of Na-incorporated C-A-S-H gels, confirming the precipitation of alkali on the surface of hydration products. In this study, the formation of the main hydration products and the $CaCO_3$ resulting from the decalcification of the C-A-S-H gel are discussed in detail. The peaks assigned to C–S–H at 29.5° (2θ) and hydrotalcite ($Mg_6Al_2(CO_3)(OH)_{16}.4H_2O$) [18,19,50] were observed in all the samples. Particularly

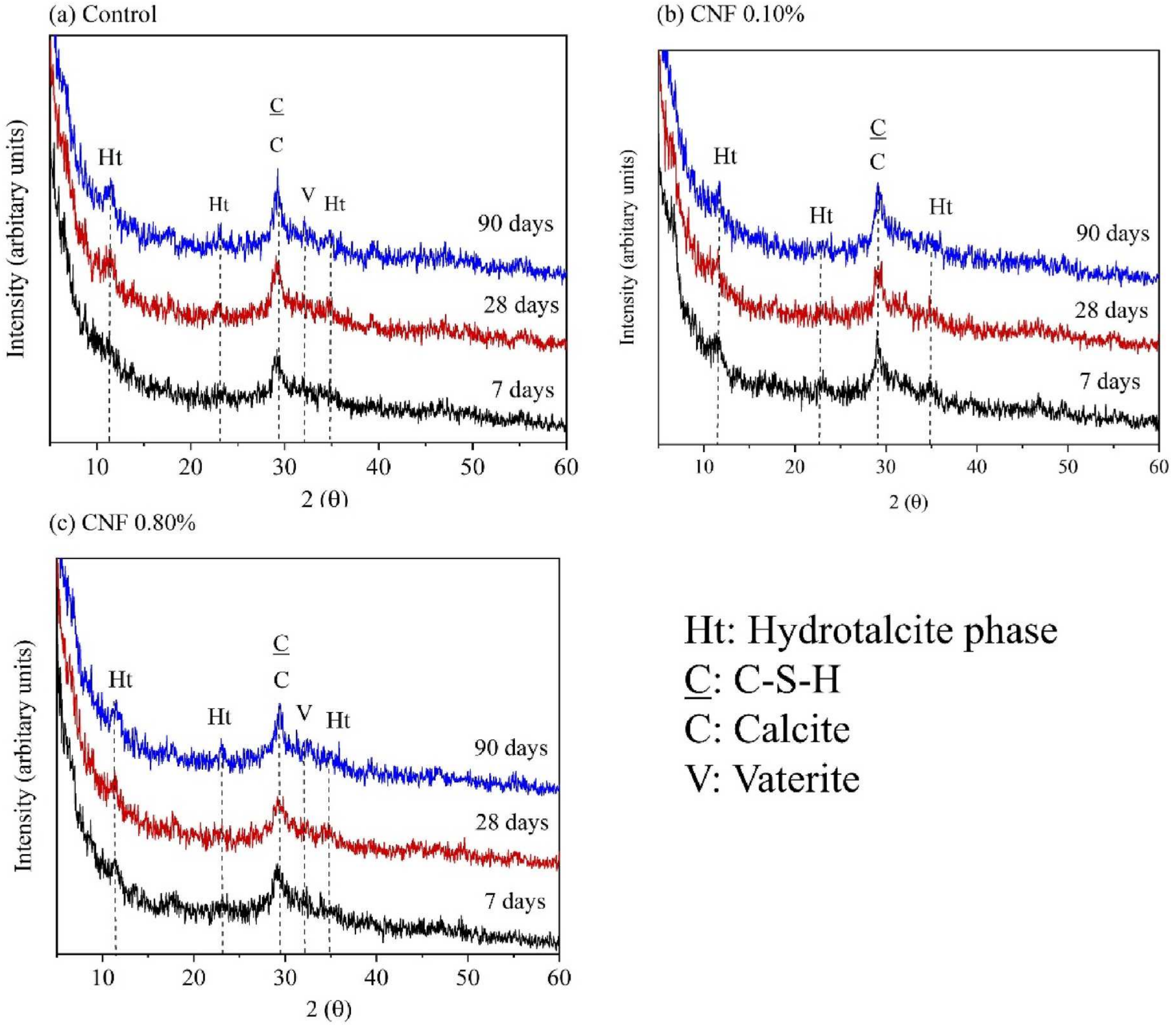

Fig. 6. XRD pattern of (a) Control (b) CNF 0.10 % and (c) CNF 0.80 % batches after 7, 28, and 90 days of natural carbonation.

the CNF 0.10 % batch, compared to the control batch, showed an amorphous hump peak of the C-A-S-H with an increase in the curing duration (Fig. 6). This conforms with the previous findings from FTIR and TGA that CNF provides additional nucleation sites for C-A-S-H growth. The C-A-S-H exhibits a lower intensity peak in the CNF 0.80 % batch. This was because, at higher dosages of this batch, the formation of C-A-S-H growth was inhibited due to the agglomeration of fibers as well as the alkali (Na) binding of CNF. As the specimen aged, it was observed that the intensity of the calcite peak at 29.42° (2θ) [19], [56] increased for all the samples. The intensity of calcite was higher in samples with lower CO_2 concentrations, especially in naturally carbonated samples, which is consistent with other literature findings [18,57].

3.3. *Effect of CNF on accelerated carbonation of alkali-activated slag*

3.3.1. *Macroscale effects*

The compressive strength of mortar samples was tested after 7, 28, and 90 days of accelerated carbonation, as shown in Fig. 7. It was observed that the compressive strength of the control batch was significantly reduced by 22.5 MPa after 7 days. This reduction was attributed to the decalcification of C-A-S-H gel into alumina-silica gel and the formation of $CaCO_3$. After 28 days of accelerated carbonation, the compressive strength of the control batch slightly increased (25.8 MPa), most likely due to the formation of $CaCO_3$ polymorphs that occupied the pores and refined their pore structure. After 90 days, the strength of the control batch decreased drastically (20.8 MPa), indicating the presence

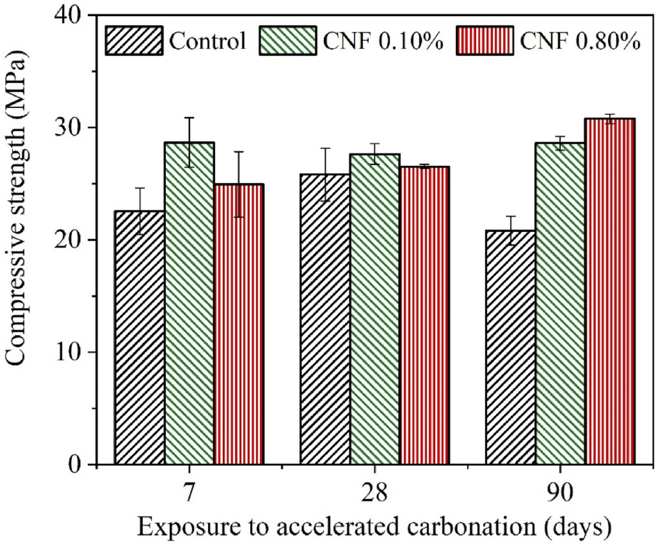

Fig. 7. Compressive strengths of control, CNF 0.10 % and CNF 0.80 % batches after 7, 28, and 90 days of accelerated carbonation.

of larger pores and a subsequent reduction in strength due to the C-A-S-H decalcification. On the other hand, the strength of the 0.1% CNF batches remained almost the same without any significant loss at 7 days (28.7 MPa), 28 days (27.6 MPa), and 90 days (28.6 MPa). Furthermore, the strength of the CNF batch with a higher dosage (0.80 % CNF) increased with the duration of exposure: 7 days (24.9 MPa), 28 days (26.5 MPa), and 90 days (30.7 MPa). Therefore, the inclusion of CNFs in an alkali-activated slag system enhances its compressive strength when exposed to accelerated carbonation. This can be attributed to the presence of fibers, which have (i) crack bridging effect [37,38] and (ii) nano-composite formation due to the negatively charged carboxylate group of CNFs binding the $CaCO_3$, which leads to an organized formation of carbonates.

(a) Control_SEC 1 (b) Control_SEC 3

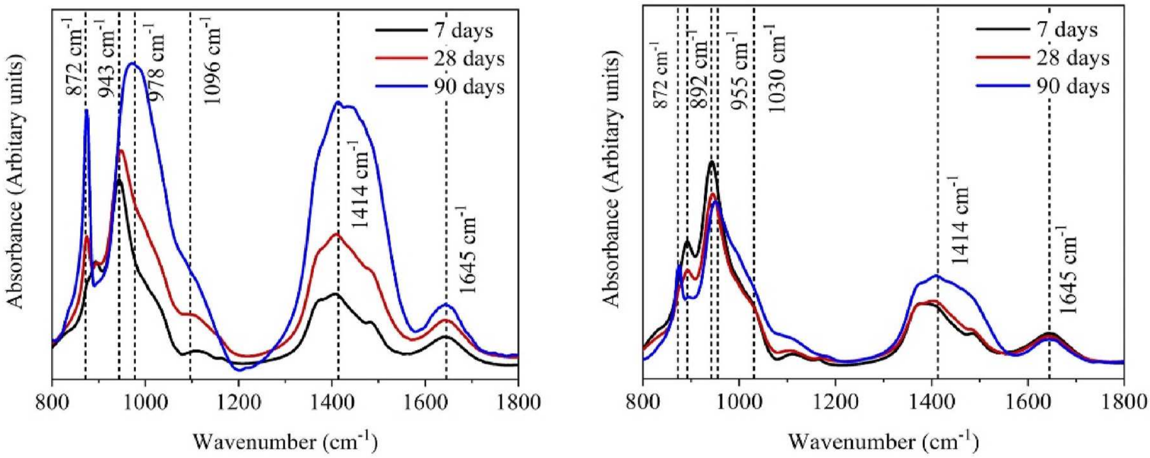

(c) CNF 0.10%_SEC 1 (d) CNF 0.10%_SEC 3

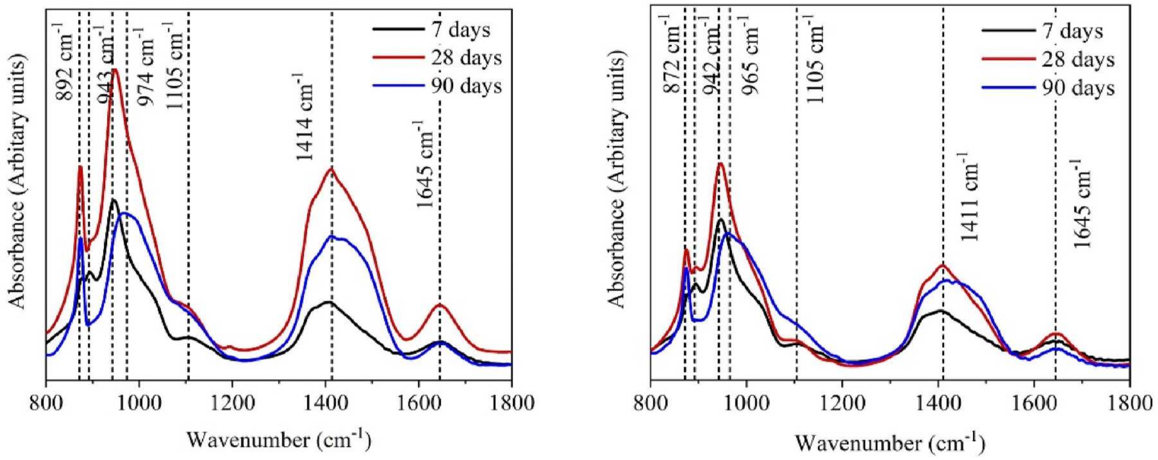

(e) CNF 0.80%_SEC 1 (f) CNF 0.80%_SEC 3

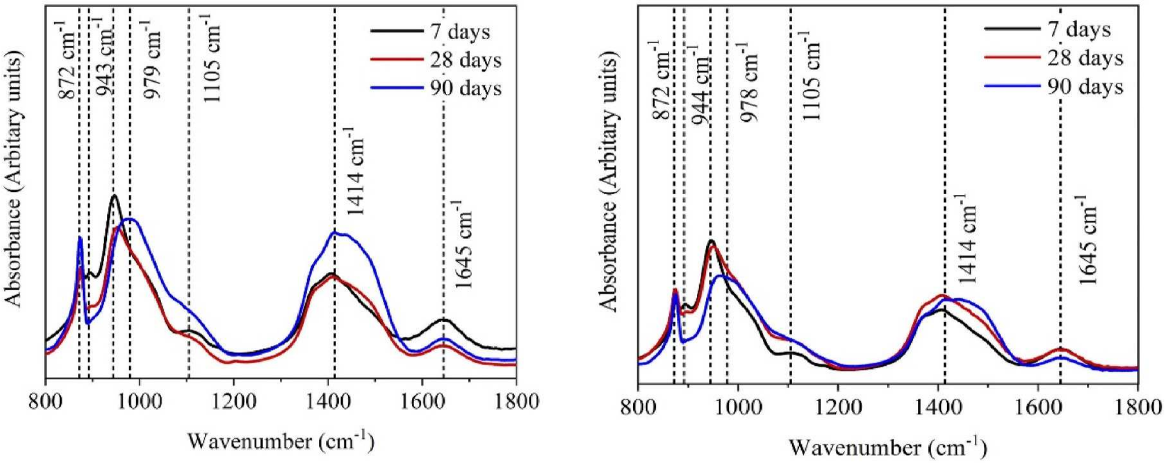

Fig. 8. FTIR spectra of (a)–(b) control SEC 1 and SEC 3; (c)–(d) CNF 0.10 % SEC 1 and SEC 3 and (e)–(f) CNF 0.80 % SEC 1 and SEC 3, batches after 7, 28, and 90 days of accelerated carbonation.

3.3.2. Microscale effect

3.3.2.1. Silicate and carbonate phase alteration due to accelerated carbonation. Fig. 8 depicts the FTIR spectra of powdered alkali-activated slag samples that were exposed to accelerated carbonation for 7, 28, and 90 days, with varying dosages of CNFs. The FTIR spectra of the exposed (SEC 1), and mid-section (SEC 3) were analyzed to determine the extent of CO_2 diffusion into the samples. For the control sample, the Q^2 peak at 940 cm^{-1} shifted to broader and higher wave numbers after three months compared to the CNF batches (Fig. 8 a). The characteristic peaks at 872 cm^{-1} and 1414 cm^{-1}, which were due to the asymmetric stretching vibration of the C–O bond in calcite, became more prominent. Thus, due to accelerated carbonation, the decalcification of the C-A-S-H gel transforms into alumina-silica gel and $CaCO_3$, specifically calcite. The mid-section (SEC 3) was not severely affected by carbonation degradation, as observed in SEC 1, due to the slow diffusivity of CO_2 inside the sample (Fig. 8 b.). In the SEC3 of the control sample, the Q^2 peak intensity gradually decreased, while a simultaneous increase in the calcite peak at 1414 cm^{-1} was observed with an increase in the duration of accelerated carbonation.

In the case of CNF 0.10 %, after 28 days of accelerated carbonation in SEC 1, there was a sharp increase in the peak at 943 cm^{-1}, along with an increase in the 872 cm^{-1} peak and 1414 cm^{-1} peak (Fig. 8 c). After three months of accelerated carbonation, the intensity of the 943 cm^{-1} peak reduced with a broad peak and an additional shoulder at 1105 cm^{-1} (Q^4) peak, indicating a higher degree of silica polymerization due to the decalcification of the C-A-S-H gel. The same pattern was observed in SEC 3 of the CNF 0.10 % batch (Fig. 8 d).

The trend of CNF 0.80 % batches (Fig. 8 e.) is similar to that of CNF 0.10 % batch, where the peak intensity at 943 cm^{-1} increased up to 28 days of accelerated carbonation. However, the peak intensity rise was not as prominent as in the CNF 0.10 % batch. Furthermore, as the exposure duration increased to 3 months, the peak broadened, indicating a shift of 943 cm^{-1} to a higher wave number (1105 cm^{-1}), which corresponds to a higher degree of polymerization due to the decalcification of the C-A-S-H gel. The characteristic calcite peak at 872 cm^{-1} and 1414 cm^{-1} peak intensity increased with the accelerated carbonation exposure duration. The observations were consistent for the mid-section (SEC 3) of the same sample (Fig. 8 f).

FTIR spectra primarily provides qualitative comparison among different samples. To quantitatively compare the extent of decalcification of different samples, we took the intensity ratios of the peaks corresponding to the C–S–H and calcite. The decalcification percentage was calculated for SEC 1 and SEC 3 for all the batches using the following equation.

$$Decalcification\ (\%) = \frac{I_{1400\ cm^{-1}}}{I_{960\ cm^{-1}}} \times 100\%$$

Here, $I_{1400\ cm\text{-}1}$ = Intensity of the peak at 1400 cm^{-1} and.

$I_{960\ cm\text{-}1}$ = Intensity of the peak at 960 cm^{-1}

This parameter allows to directly compare the relative amounts of C-A-S-H and $CaCO_3$ present in the carbonated matrix. A higher decalcification percentage indicates relatively more carbonate formation in the matrix compared to the C–S–H gel. From the experiment, it was noted that SEC 1 had a higher decalcification percentage when subjected to accelerated carbonation (Fig. 9 a). After 7 days of exposure, the order of decalcification percentage was CNF 0.80 % > Control > CNF 0.10 %, with age of specimens being a factor. However, after three months, all the batches showed nearly the same level of decalcification in SEC 1. Contradictorily, the decalcification percentages were significantly different among the batches in SEC 3, indicating different CO_2 diffusion rates in these matrixes (Fig. 9 b). In SEC 3, the order of decalcification was CNF 0.80 % > CNF 0.10 % > control batch. This may be attributed to the short-circuit diffusion mechanism proposed to explain the improved hydration of CNF-containing composites of CNF fibers [39]. Through this mechanism, the CNF fibers may have facilitated the diffusion of bicarbonate ions (HCO_3^-) within the C–S–H gels accelerating their decalcification. Interesting to note, even though the addition of CNF accelerated the carbonate formation, the compressive strength of the CNF-containing batches did not show any significant reduction even after prolonged exposure to accelerated carbonation.

The TGA plot of powdered alkali-activated slag samples subjected to accelerated carbonation for 7, 28, and 90 days with varying doses of CNFs has been shown in Fig. 10. To evaluate the level of CO_2 diffusion into the alkali-activated slag system, the TGA plots were analyzed for both the exposed (SEC 1) and mid-section (SEC 3), as illustrated in Fig. 10. For the control batch, the weight loss intensity peak between 20 and 200 °C, which was caused by the decomposition of C-A-S-H gel, reduced with accelerated exposure duration (Fig. 10 a and b), a similar trend to natural carbonation. This was confirmed by the weight loss percentage increase within temperatures of 600–700 °C and 750–850 °C as the specimens age.

For CNF 0.10 %, in SEC 1, the weight loss percentage between the 20–200 °C intensity peak at 28 days was slightly lower compared to the 7 days, indicating a higher level of decalcification with increasing duration (Fig. 10 c). However, in SEC 3, there was not any significant difference in this temperature range between 7 and 28 days of carbonation (Fig. 10 d). This indicates that after the carbonation up to 7 days,

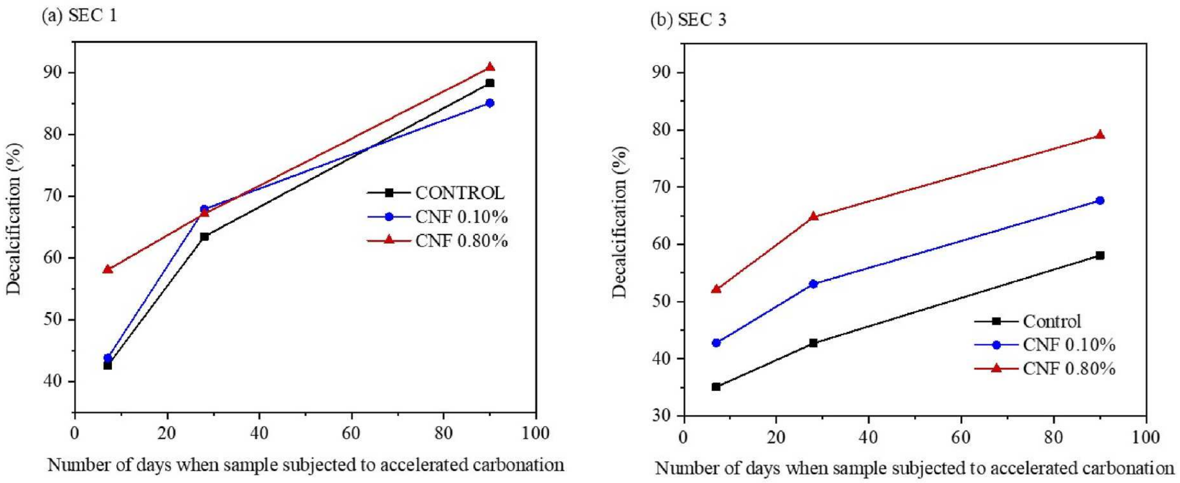

Fig. 9. Decalcification (%) of (a) exposed face (SEC 1) and (b) mid-section (SEC3) of samples subjected to accelerated carbonation.

(a) Control_SEC 1 (b) Control_SEC 3

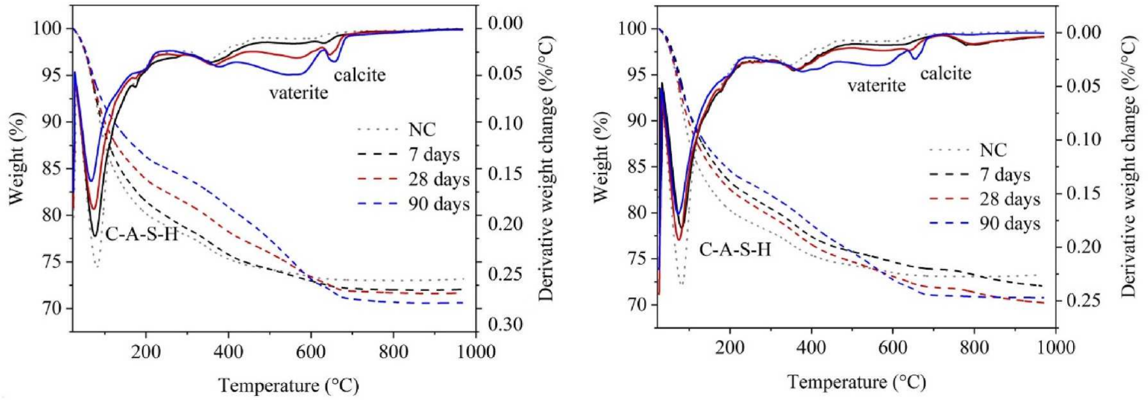

(c) CNF 0.10%_SEC 1 (d) CNF 0.10%_SEC 3

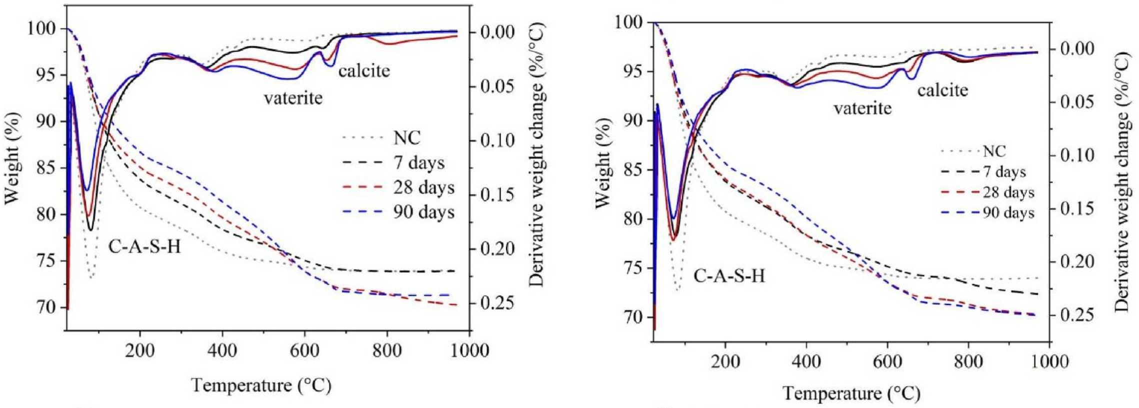

(e) CNF 0.80%_SEC 1 (f) CNF 0.80%_SEC 3

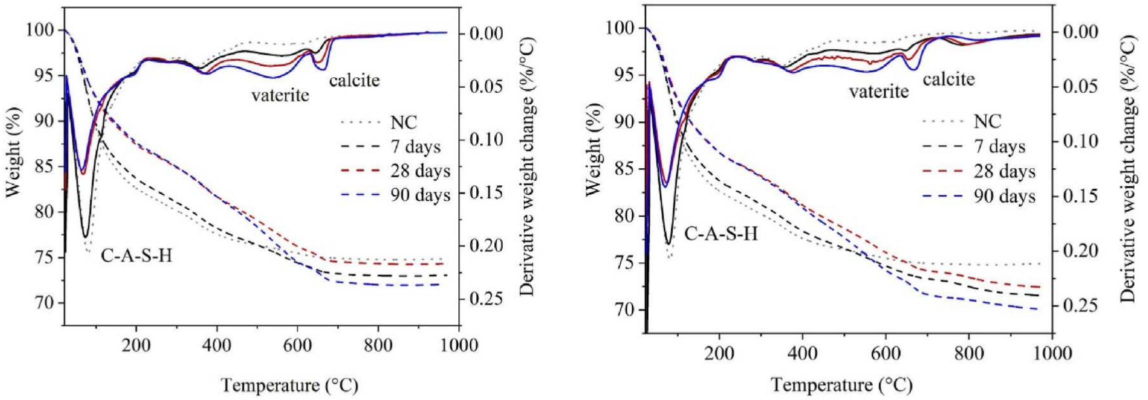

Fig. 10. TGA plots of (a)–(b) control SEC 1 and SEC 3; (c)–(d) CNF 0.10 % SEC 1 and SEC 3 and (e)–(f) CNF 0.80 % SEC 1 and SEC 3, batches after 7, 28, and 90 days of accelerated carbonation; NC – natural carbonated sample after 28 days.

the further carbonation of the matrix (SEC 3) was reduced due to the slower CO_2 ingress. The reduced CO_2 ingress resulted from the pore blocking effects of precipitated $CaCO_3$. The weight loss percentage increases at temperatures of 600–700 °C and 750–850 °C, and the age of the specimen in both sections with vaterite content predominant was the same as in the control sample.

The weight loss peak of CNF 0.80 % between 20 and 200 °C reduced significantly after carbonation for 7 days, and there was not much change after 28 and 90 days (Fig. 10 e). This indicates that decalcification was prominent after 7 days, and then stabilized as it aged. This was also evident from the weight loss due to $CaCO_3$ polymorphs at 600–700 °C and 750–850 °C as the specimen aged. Similar observations were made in SEC 3 (Fig. 10 f). The compressive strength results of CNF 0.80 % also showed an improvement after 28 days and especially after 3 months of accelerated carbonation. The accelerated rate of carbonation of CNF 0.80 % can be due to the increased porosity resulting from the fiber agglomerations. However, these observations further confirm that the addition of CNF accelerated the carbonation of AAS, without negatively affecting the compressive strength of the matrix.

In order to better understand the CO_2 sequestration of CNF in AAS system, carbonation quantification was done. The TGA plots were used to quantify the C-A-S-H gel (%) between 20 °C and 200 °C before exposure (represented as zero days in (Fig. 11 a and b) and after accelerated carbonation durations. The $CaCO_3$ (%) was calculated within the temperature range of 400 °C to 800 °C after accelerated carbonation (Fig. 11 c and d). This provided insight into the impact of CO_2 diffusion in the AAS paste samples.

The results showed that after 28 days of accelerated carbonation,

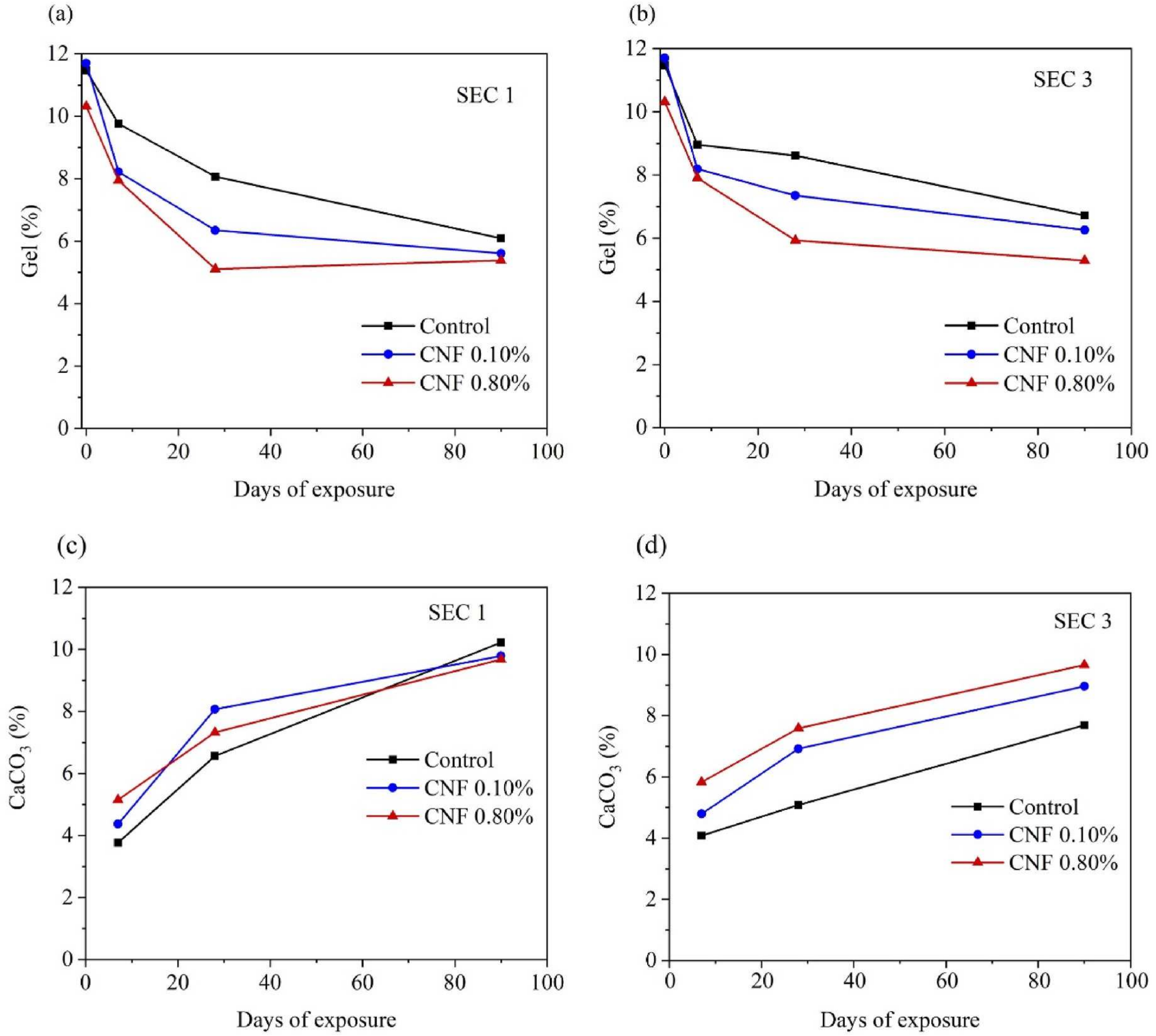

Fig. 11. (a)–(b) Gel (%); (c)–(d) $CaCO_3$ quantification of the exposed face (SEC 1) and mid-section (SEC3) of samples subjected to accelerated carbonation.

SEC 3 had a higher gel (%) than SEC 1 for all batches. The $CaCO_3$ (%) content was also lower for SEC 3 than SEC 1, with the exception of CNF 0.80 %. This was expected as SEC 1 was directly exposed to CO_2 and the carbonation at SEC 3 depended on the CO_2 diffusion into the matrix. After 90 days of accelerated carbonation, the same trend as that of 28 days for the gel (%) and $CaCO_3$ (%) was observed for the control and CNF 0.10 %. It was observed that for the control batch, SEC 1 had more $CaCO_3$ (%) than CNF 0.10 %. However, in SEC 3, it was observed that both CNF doses had a higher percentage of $CaCO_3$ than the control batch. This confirms previous FTIR findings that the addition of CNF accelerated carbonate formation without compromising the compressive strength of AAS samples. Specifically, the CNF 0.10 % batch showed 18.4 % more $CaCO_3$ formation at SEC 3 compared to the control batch. Thus, the addition of 0.1 % CNF increased the CO_2 sequestration in AAS by 18.4 %.

The XRD pattern of powdered alkali-activated slag samples from two sections (SEC 1 and SEC 3) subjected to accelerated carbonation of control, CNF 0.10 %, and CNF 0.80 % for 7, 28, and 90 days is shown in Fig. 12. During the experiment, it was noticed that in the control batch, upon accelerated carbonation, the intensity of the amorphous hump peak of C–S–H was reduced; simultaneously, a sharp peak intensity of calcite became more prominent, indicating the decalcification (Fig. 12 a). The presence of vaterite becomes more distinct with an increased duration of accelerated carbonation. After 90 days of accelerated carbonation, the peak intensity of vaterite was observed to be almost equal to that of calcite (Fig. 12 a). Studies have found that vaterite is the primary product resulting from exposure to elevated CO_2 levels, increasing with curing time and CO_2 concentration [18,57,58]. Calcite is most prominent at high RH, while all three polymorphs of $CaCO_3$ coexist at intermediate RH. The least stable polymorph of $CaCO_3$ tends to crystallize first, leading to the observation of the metastable $CaCO_3$ polymorphs vaterite and aragonite at high CO_2 concentrations, whereas calcite is the primary carbonation product in natural carbonated specimens [18,57,58]. It has been observed that there was a significant difference in the intensity of the vaterite peak between the carbon-dioxide-facing section (SEC 1) (Fig. 12 c) and the mid-section (SEC 3) (Fig. 12 d) of the CNF 0.10 % batch. The vaterite peak intensity in SEC 3 was comparatively lower due to the lesser extent of carbonation at this section. Additionally, the formation of additional C-A-S-H caused a delay in the carbonation degradation of the specimen. The intensity of the calcite peak was found to be significantly increased even after 7 days and continued to increase up to 3 months of accelerated carbonation in the case of CNF 0.80 % (Fig. 12 e and f). However, the peak intensities were still lower as compared to both control and CNF 0.10 % in natural carbonation.

3.3.2.2. Pore size distribution of samples subjected to natural and accelerated carbonation.

Fig. 13 depicts the (a) cumulative porosity as a

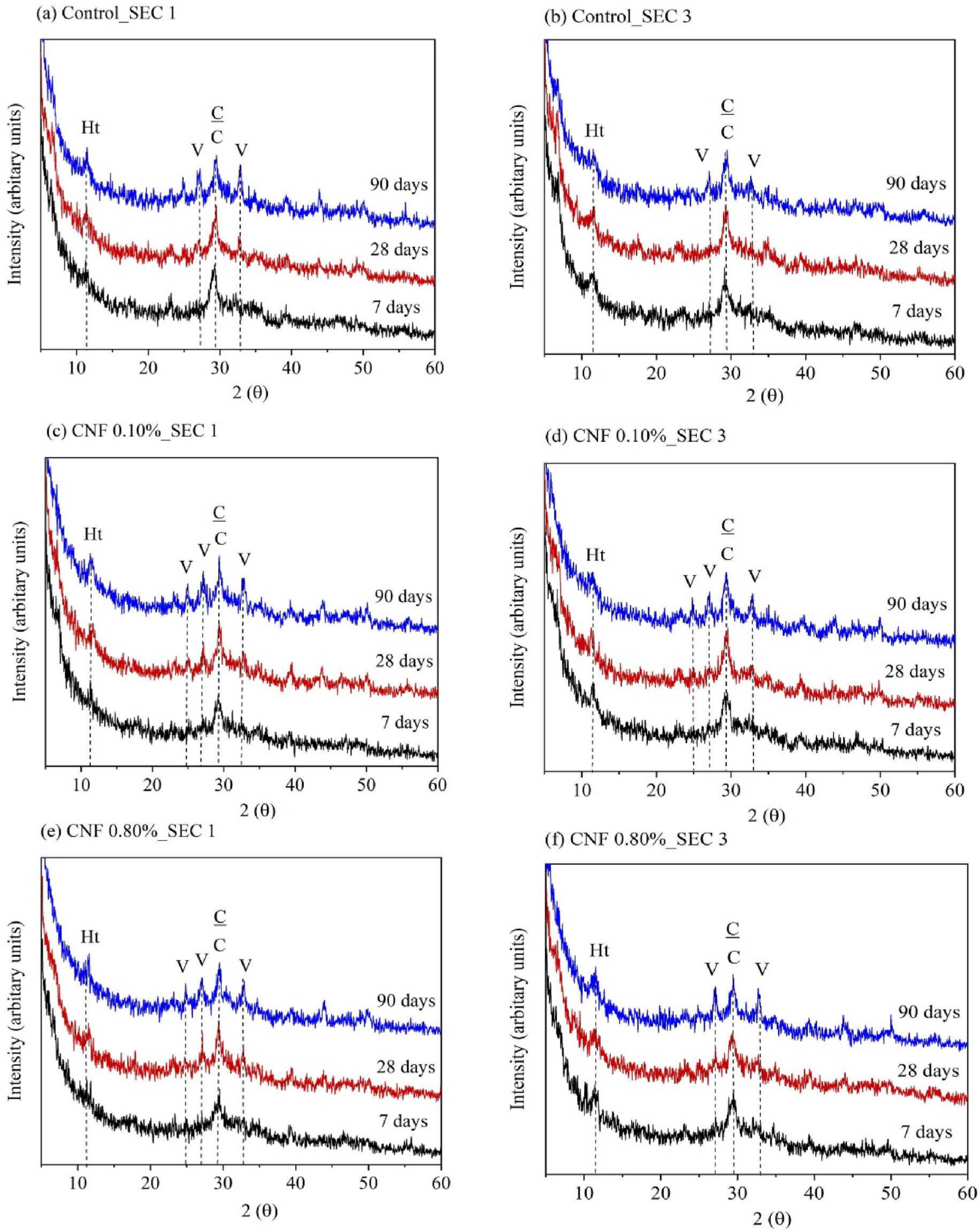

Fig. 12. XRD spectra of (a)–(b) control SEC 1 and SEC 3; (c)–(d) CNF 0.10 % SEC 1 and SEC 3 and (e)–(f) CNF 0.80 % SEC 1 and SEC 3, batches after 7, 28, and 90 days of accelerated carbonation; Ht: Hydrotalcite phase, C: C–S–H, C: Calcite; V-Vaterite.

function of pore diameter and (b) pore size distribution, after 28 days of natural carbonation and 90 days of accelerated carbonation. The total porosity and average pore diameter data obtained from Mercury Intrusion Porosimetry (MIP) analysis are summarized in Table 3. After 28 days of natural carbonation, the control batch exhibits notably higher porosity (14.74 %) than the CNF 0.10 % batch (8.81 %). The pore size distribution, shown in Fig. 13 b, indicates that the control batch exhibits a broader range of porosity. These findings align with the results discussed in section 3.2, which showed that the incorporation of CNFs facilitated additional C-A-S-H formation and enhanced the binding of $CaCO_3$ polymorphs, thereby refining the pore structure and densifying the microstructure.

When the samples were subjected to accelerated carbonation, a noticeable shift in pore distribution was observed for both batches, as shown in Fig. 13 a. and b. Unlike in natural carbonation, the total porosity of the control batch (9.53 %) was lower compared to the CNF 0.10 % batch (11.15 %) for accelerated carbonation. This reduction can be attributed to the precipitation of $CaCO_3$, which occupies the empty

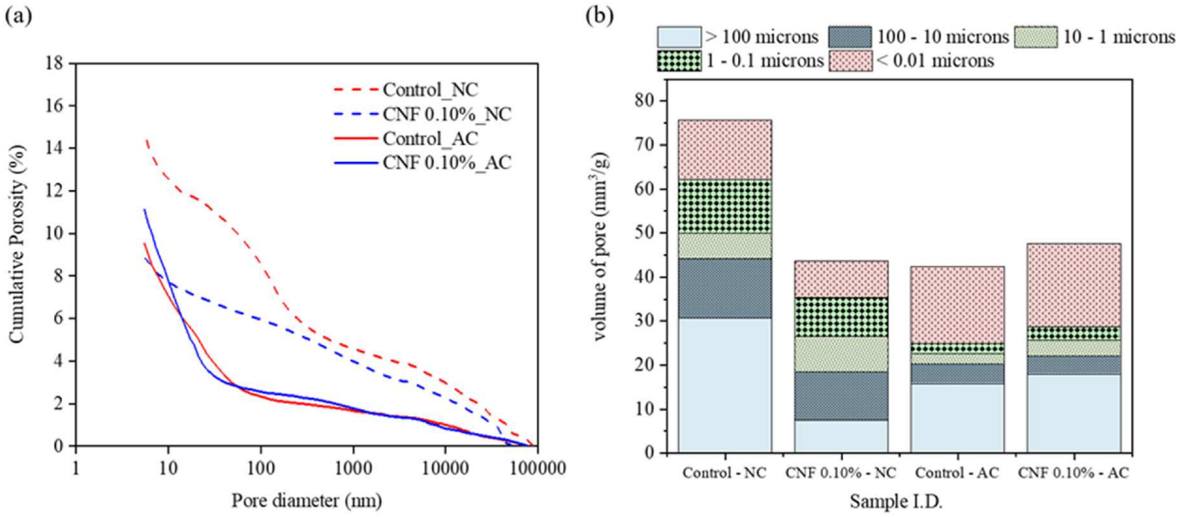

Fig. 13. (a) Cumulative intrusion curve and (b) pore size distribution of Control and CNF 0.10 % under natural carbonation (NC) at 28 days and accelerated carbonation (AC) after 90 days.

Table 3
Summarized MIP results of Natural (NC) and Accelerated carbonation (AC).

	Total porosity (%)		Average pore diameter (nm)	
	Control	CNF 0.10 %	Control	CNF 0.10 %
NC	14.74	8.81	50.2	41.9
AC	9.53	11.15	23.9	20.3

pore space in the microstructure. Consequently, the overall porosity of the sample was reduced upon accelerated carbonation. The CNF 0.10 % batch showed an increase in porosity following accelerated carbonation. However, considering the size distribution (Fig. 13 b), the volume of pores in the size range of 0.1–100 μm was reduced and the volume of pores smaller than 0.1 μm (100 nm) were increased. The increase in this nano porosity range indicates pore refinement of the CNF sample despite the increase in total porosity. Notably, the average pore diameter of the CNF 0.10 % sample was also smaller than the control. Consequently, the compressive strength remains uncompromised despite the observed microstructural modifications, as explained in section 3.3.1.

3.3.2.3. SEM observations of AAS samples under accelerated carbonation. The Backscattered Electron (BSE) images showed significant changes in the microstructure of the samples assessed, which were subjected to 90 days of accelerated carbonation exposure (Fig. 14). As previously discussed, the carbonation and decalcification of C–A–S–H gel caused the formation of silica gel and $CaCO_3$. Consequently, the matrix loses continuity, primarily attributed to the decalcification of the C-A-S-H gel. In the control batch, Fig. 14 a and b, the impact of carbonation degradation was evident through the presence of microporosity and observable microcracks, as indicated by the marked regions in the images. The formation of these microcracks was a consequence of carbonation shrinkage associated with the decalcification of the C-A-S-H gel. This coarsening of the microstructure is a contributing factor to the decline in compressive strength observed in AAS systems undergoing carbonation degradation.

The microstructure of AAS samples containing 0.10 % CNFs (Fig. 14 c and d) were denser compared to the control batch. In these images, the darker grey region shows the decalcified silica gel and lighter grey is the $CaCO_3$. Nearly the whole microstructure was carbonated. However, compared to the control batch, a lesser number of microcracks were observed. Additionally, no agglomerations of CNF were observed in the SEM BSE images. These images show that the carbonation of CNF 0.10 % batch resulted in a refined and denser microstructure, ultimately enhancing the compressive strength of the AAS samples. The BSE images of the 90 days carbonated CNF 0.80 % samples (Fig. 14 e and f) show fiber agglomerations throughout the microstructure. However, an interesting observation is that the $CaCO_3$ preferentially deposited on the fibers as marked in Fig. 14 f. This was further confirmed by the secondary images of the fractured samples as shown in Fig. 15 a. and b. This indicates that CNFs effectively bind with the $CaCO_3$, which enables a more organized precipitation of this phase. This helps refine the pore structure to some extent, which aids in retaining and slightly improving the compressive strength even after 90 days of exposure.

The above-discussed experimental findings revealed that the addition of CNF enables CO_2 sequestration in AAS without causing mechanical performance (i.e., compressive strength) degradation. However, one potential limitation of this approach is that the CO_2 sequestration in AAS might lead to a significant reduction in the alkalinity of the pore solution. This decrease in alkalinity could, in turn, increase the susceptibility of the reinforcement to corrosion. While such a corrosion mechanism is well-documented for OPC-based composites, it remains unclear whether similar effects would occur in alkali-activated slag systems. Consequently, additional investigations are required to thoroughly assess the potential for reinforcement corrosion in alkali-activated slag due to CO_2 sequestration and to determine the extent of its impact on the durability and long-term performance of these composites.

4. Conclusions

This study investigated the effect of CNF on natural and accelerated carbonations of alkali-activated slag. Two different dosages of CNFs by weight of slag were used in this study. The AAS was subjected to natural and accelerated carbonation. The macroscale and microstructural effects due to carbonation were examined. The major conclusions of this study are as follows:

- The inclusion of CNF in alkali-activated slag (AAS) initially caused a slight delay in compressive strength development at 7 days compared to the control sample. However, by 28 days, the compressive strength improved and exceeded that of the control batch. The negatively charged carboxyl surface sites of CNFs can get adsorbed on the slag particle causing an initial delay in the dissolution of the AAS binder. Over time, however, CNFs generate nucleation sites, leading to the formation of additional C-A-S-H. Despite

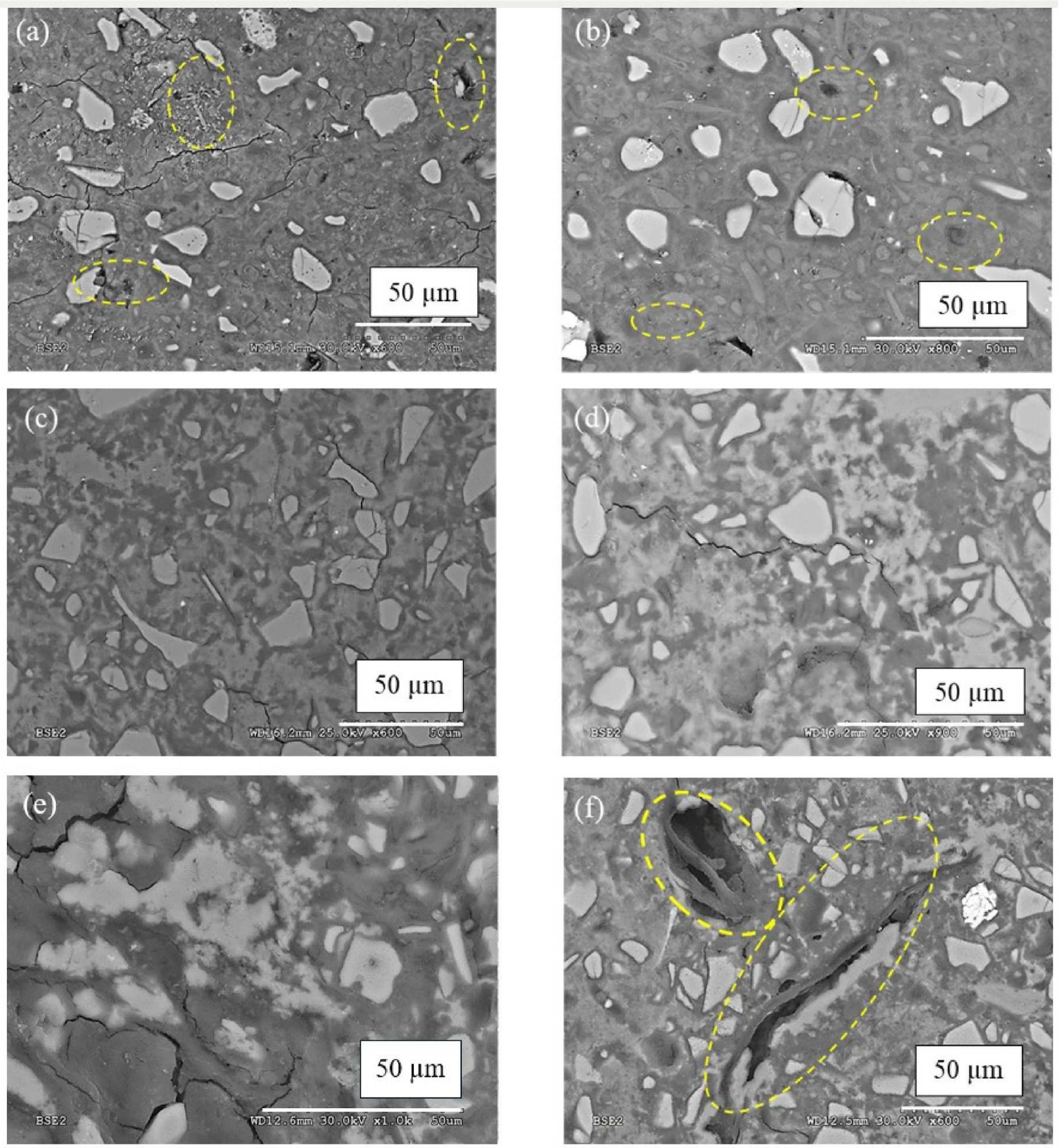

Fig. 14. Backscattered electron images of (a)–(b) control; (c)–(d) CNF 0.10 % and (e)–(f) CNF 0.80 %, batch after 90 days of accelerated carbonation.

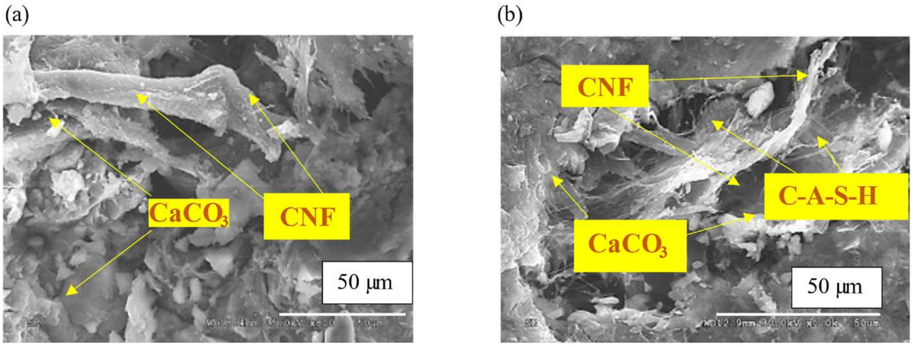

Fig. 15. Secondary electron images of (a)–(b) CNF 0.10 % batch.

this benefit, a higher concentration of CNFs can result in the agglomeration of fibers, which increases porosity and lowers compressive strength.
- After 90 days of natural carbonation, the control batch exhibited a reduction in compressive strength, whereas the CNF batches showed an enhancement. Notably, the CNF-containing batches maintained consistent strength over time, with no reduction in strength.
- Microstructural analyses of the naturally carbonated samples revealed that in all batches, the decalcification of calcium-alumino-silicate-hydrate (C-A-S-H) gel led to the formation of highly polymerized silica gel and calcium carbonate ($CaCO_3$) polymorphs. Calcite is the main $CaCO_3$ polymorph observed in all samples.
- After 90 days of accelerated carbonation, CNF 0.10 % and CNF 0.80 % showed an increase in compressive strength compared to the control batch. Despite this enhancement in compressive strength, microstructural studies showed that the CNF-containing samples experienced a higher extent of carbonation than the control batch after 90 days of accelerated carbonation. Specifically, 0.1 % and 0.8 % addition of CNF resulted in 18.4 % and 30.2 % higher CO_2 sequestration, respectively, compared to the control batch.
- The enhancement in compressive strength of CNF due to carbonation has been further elucidated through MIP and SEM/BSE analysis. MIP results indicated that the control and CNF-containing samples showed pore refinement due to accelerated carbonation. However, the SEM/BSE images of the accelerated carbonated samples showed that the control batch had significantly more microcracks than the CNF 0.1 % batch. The increased porosity due to these microcracks resulted in the reduction in compressive strength of the control batch. In contrast, the CNF batches exhibited a nano-composite structure with $CaCO_3$ polymorphs, which mitigated microcrack formation and refined the pore structure. This structural pore refinement contributed to the increase in compressive strength, despite the extent of carbonation.

In summary, the addition of CNF resulted in a higher degree of carbonation of AAS, but without causing a degradation of their compressive strengths. This approach of modifying AAS with abundantly available biopolymers offers a novel pathway for sequestering CO_2 in alkali-activated materials without performance degradation.

CRediT authorship contribution statement

Nithya Nair: Writing – review & editing, Writing – original draft, Formal analysis, Data curation, Conceptualization. **Warda Ashraf:** Writing – review & editing, Supervision, Project administration, Funding acquisition, Data curation, Conceptualization.

Declaration of competing interest

The authors declare that no conflict of interest is involved in this paper and the authors are responsible for the content and writing.

Data availability

Data will be made available on request.

Acknowledgments

Funding for this research was provided by the US National Science Foundation (NSF # ECI -2028462). All opinions, findings, and conclusions or recommendations expressed in this material are those of the authors and do not necessarily reflect the views of the funding agencies.

References

[1] J.G.J. Olivier, J.A.H.W. Peters, TRENDS IN GLOBAL CO 2 AND TOTAL GREENHOUSE GAS EMISSIONS 2018 Report Trends in global CO2 and total greenhouse gas emissions: 2018 Report [Online]. Available: www.pbl.nl/en, 2018.

[2] A. Komkova, G. Habert, Environmental impact assessment of alkali-activated materials: examining impacts of variability in constituent production processes and transportation, Construct. Build. Mater. 363 (Jan) (2023), https://doi.org/10.1016/j.conbuildmat.2022.129032.

[3] T. Bakharev, Durability of geopolymer materials in sodium and magnesium sulfate solutions, Cement Concr. Res. 35 (6) (Jun. 2005) 1233–1246, https://doi.org/10.1016/j.cemconres.2004.09.002.

[4] P. Duxson, J.L. Provis, G.C. Lukey, S.W. Mallicoat, W.M. Kriven, J.S.J. Van Deventer, Understanding the relationship between geopolymer composition, microstructure and mechanical properties, Colloids Surf. A Physicochem. Eng. Asp. 269 (1–3) (Nov. 2005) 47–58, https://doi.org/10.1016/j.colsurfa.2005.06.060.

[5] T. Bakharev, Resistance of geopolymer materials to acid attack, Cement Concr. Res. 35 (4) (Apr. 2005) 658–670, https://doi.org/10.1016/j.cemconres.2004.06.005.

[6] D.L.Y. Kong, J.G. Sanjayan, Damage behavior of geopolymer composites exposed to elevated temperatures, Cem. Concr. Compos. 30 (10) (Nov. 2008) 986–991, https://doi.org/10.1016/j.cemconcomp.2008.08.001.

[7] D. Ravikumar, S. Peethamparan, N. Neithalath, Structure and strength of NaOH activated concretes containing fly ash or GGBFS as the sole binder, Cem. Concr. Compos. 32 (6) (Jul. 2010) 399–410, https://doi.org/10.1016/j.cemconcomp.2010.03.007.

[8] J. Shi, J. Ming, M. Wu, Passivation and corrosion behavior of 2304 duplex stainless steel in alkali-activated slag materials, Cem. Concr. Compos. 108 (Apr) (2020), https://doi.org/10.1016/j.cemconcomp.2020.103532.

[9] W. Aperador, R. Mejía de Gutiérrez, D.M. Bastidas, Steel corrosion behaviour in carbonated alkali-activated slag concrete, Corrosion Sci. 51 (9) (Sep. 2009) 2027–2033, https://doi.org/10.1016/j.corsci.2009.05.033.

[10] J. Shi, J. Ming, W. Sun, Electrochemical performance of reinforcing steel in alkali-activated slag extract in the presence of chlorides, Corrosion Sci. 133 (Apr. 2018) 288–299, https://doi.org/10.1016/j.corsci.2018.01.043.

[11] X. Ke, M. Criado, J.L. Provis, S.A. Bernal, Slag-based cements that resist damage induced by carbon dioxide, ACS Sustain. Chem. Eng. 6 (4) (Apr. 2018) 5067–5075, https://doi.org/10.1021/acssuschemeng.7b04730.

[12] M. Palacios, F. Puertas, Effect of carbonation on alkali-activated slag paste, J. Am. Ceram. Soc. 89 (10) (Oct. 2006) 3211–3221, https://doi.org/10.1111/j.1551-2916.2006.01214.x.

[13] F. Puertas, M. Palacios, T. Vázquez, Carbonation process of alkali-activated slag mortars, J. Mater. Sci. 41 (10) (May 2006) 3071–3082, https://doi.org/10.1007/s10853-005-1821-2.

[14] J.L. Provis, Alkali-activated materials, Cement Concr. Res. 114 (Dec. 01, 2018) 40–48, https://doi.org/10.1016/j.cemconres.2017.02.009. Elsevier Ltd.

[15] S.A. Bernal, R.M. de Gutierrez, J.L. Provis, V. Rose, Effect of silicate modulus and metakaolin incorporation on the carbonation of alkali silicate-activated slags, Cement Concr. Res. 40 (6) (Jun. 2010) 898–907, https://doi.org/10.1016/j.cemconres.2010.02.003.

[16] S.A. Bernal, J.L. Provis, V. Rose, R. Mejía De Gutierrez, Evolution of binder structure in sodium silicate-activated slag-metakaolin blends, Cem. Concr. Compos. 33 (1) (Jan. 2011) 46–54, https://doi.org/10.1016/j.cemconcomp.2010.09.004.

[17] S.A. Bernal, J.L. Provis, D.G. Brice, A. Kilcullen, P. Duxson, J.S.J. Van Deventer, Accelerated carbonation testing of alkali-activated binders significantly underestimates service life: the role of pore solution chemistry, Cement Concr. Res. 42 (10) (Oct. 2012) 1317–1326, https://doi.org/10.1016/j.cemconres.2012.07.002.

[18] S.A. Bernal, et al., Gel nanostructure in alkali-activated binders based on slag and fly ash, and effects of accelerated carbonation, Cement Concr. Res. 53 (2013) 127–144, https://doi.org/10.1016/j.cemconres.2013.06.007.

[19] S.A. Bernal, et al., MgO content of slag controls phase evolution and structural changes induced by accelerated carbonation in alkali-activated binders, Cement Concr. Res. 57 (Mar. 2014) 33–43, https://doi.org/10.1016/j.cemconres.2013.12.003.

[20] R.I. Khan, M.I. Haque, W. Ashraf, S. Shah, N. Saleh, Role of biopolymers in enhancing multiscale characteristics of carbonation-cured cementitious composites, Cem. Concr. Compos. 134 (Nov) (2022), https://doi.org/10.1016/j.cemconcomp.2022.104766.

[21] R.I. Khan, W. Ashraf, J. Olek, Amino acids as performance-controlling additives in carbonation-activated cementitious materials, Cement Concr. Res. 147 (Sep) (2021), https://doi.org/10.1016/j.cemconres.2021.106501.

[22] S.A. Bernal, Microstructural changes induced by CO2 exposure in alkali-activated slag/metakaolin pastes, Front Mater 3 (Sep) (2016), https://doi.org/10.3389/fmats.2016.00043.

[23] B. Wu, G. Ye, Development of porosity of cement paste blended with supplementary cementitious materials after carbonation, Construct. Build. Mater. 145 (Aug. 2017) 52–61, https://doi.org/10.1016/j.conbuildmat.2017.03.176.

[24] W. Chen, H.J.H. Brouwers, The hydration of slag, part 1: reaction models for alkali-activated slag, J. Mater. Sci. 42 (2) (Jan. 2007) 428–443, https://doi.org/10.1007/s10853-006-0873-2.

[25] A.E. Morandeau, C.E. White, Role of magnesium-stabilized amorphous calcium carbonate in mitigating the extent of carbonation in alkali-activated slag, Chem. Mater. 27 (19) (Sep. 2015) 6625–6634, https://doi.org/10.1021/acs.chemmater.5b02382.

[26] S.Y. Wang, E. McCaslin, C.E. White, Effects of magnesium content and carbonation on the multiscale pore structure of alkali-activated slags, Cement Concr. Res. 130 (Apr) (2020), https://doi.org/10.1016/j.cemconres.2020.105979.

[27] J. He, Q. Gao, Y. Wu, J. He, X. Pu, Study on improvement of carbonation resistance of alkali-activated slag concrete, Construct. Build. Mater. 176 (Jul. 2018) 60–67, https://doi.org/10.1016/j.conbuildmat.2018.04.117.

[28] A. Isogai, L. Bergström, Preparation of Cellulose Nanofibers Using Green and Sustainable Chemistry, 2018.

[29] H.H. Kolour, W. Ashraf, E.N. Landis, Hydration and early age properties of cement pastes modified with cellulose nanofibrils, Transport. Res. Rec. 2675 (9) (2021) 38–46, https://doi.org/10.1177/0361198120945993. SAGE Publications Ltd.

[30] H.H. Kolour, M. Ahmed, E. Alyaseen, E.N. Landis, An investigation on the effects of cellulose nanofibrils on the performance of cement paste and concrete, Adv Civ Eng Mater 7 (1) (Sep. 2018) 463–478, https://doi.org/10.1520/ACEM20180048.

[31] L. Jiao, M. Su, L. Chen, Y. Wang, H. Zhu, H. Dai, Natural cellulose nanofibers as sustainable enhancers in construction cement, PLoS One 11 (12) (Dec. 2016), https://doi.org/10.1371/journal.pone.0168422.

[32] S. Parveen, S. Rana, R. Fangueiro, M.C. Paiva, A novel approach of developing micro crystalline cellulose reinforced cementitious composites with enhanced microstructure and mechanical performance, Cem. Concr. Compos. 78 (Apr. 2017) 146–161, https://doi.org/10.1016/j.cemconcomp.2017.01.004.

[33] K.S. Kamasamudram, W. Ashraf, E.N. Landis, Cellulose nanofibrils with and without nanosilica for the performance enhancement of Portland cement systems, Construct. Build. Mater. 285 (May 2021), https://doi.org/10.1016/j.conbuildmat.2020.121547.

[34] K.S. Kamasamudram, W. Ashraf, E.N. Landis, Cellulose nanocomposites for performance enhancement of ordinary portland cement-based materials, Transport. Res. Rec. 2675 (9) (2021) 11–20, https://doi.org/10.1177/0361198120958421. SAGE Publications Ltd.

[35] K.S. Kamasamudram, W. Ashraf, E.N. Landis, R.I. Khan, Effects of ligno– and delignified– cellulose nanofibrils on the performance of cement-based materials, J. Mater. Res. Technol. 13 (Jul. 2021) 321–335, https://doi.org/10.1016/j.jmrt.2021.04.090.

[36] N. Nair, et al., Role of delignified and lignin-containing cellulose nanofibers in enhancing durability performances of portland cement composites, Cem. Concr. Compos. 145 (Jan) (2024), https://doi.org/10.1016/j.cemconcomp.2023.105316.

[37] O. Onuaguluchi, D.K. Panesar, M. Sain, Properties of nanofibre reinforced cement composites, Construct. Build. Mater. 63 (Jul. 2014) 119–124, https://doi.org/10.1016/j.conbuildmat.2014.04.072.

[38] S.J. Peters, T.S. Rushing, E.N. Landis, T.K. Cummins, Nanocellulose and microcellulose fibers for concrete, Transport. Res. Rec. 2142 (Jan. 2010) 25–28, https://doi.org/10.3141/2142-04.

[39] Y. Cao, P. Zavaterri, J. Youngblood, R. Moon, J. Weiss, The influence of cellulose nanocrystal additions on the performance of cement paste, Cem. Concr. Compos. 56 (Aug. 2015) 73–83, https://doi.org/10.1016/j.cemconcomp.2014.11.008.

[40] Z. Zhang, U. Angst, Microstructure and moisture transport in carbonated cement-based materials incorporating cellulose nanofibrils, Cement Concr. Res. 162 (Dec. 2022), https://doi.org/10.1016/j.cemconres.2022.106990.

[41] R.I. Khan, M.I. Haque, W. Ashraf, S. Shah, N. Saleh, Role of biopolymers in enhancing multiscale characteristics of carbonation-cured cementitious composites, Cem. Concr. Compos. 134 (Nov) (2022), https://doi.org/10.1016/j.cemconcomp.2022.104766.

[42] H. Ez-zaki, et al., Influence of cellulose nanofibrils on the rheology, microstructure and strength of alkali activated ground granulated blast-furnace slag: a comparison with ordinary Portland cement, Materials and Structures/Materiaux et Constructions 54 (1) (Feb. 2021), https://doi.org/10.1617/s11527-020-01614-5.

[43] W. Ashraf, J. Olek, Carbonation behavior of hydraulic and non-hydraulic calcium silicates: potential of utilizing low-lime calcium silicates in cement-based materials, J. Mater. Sci. 51 (13) (Jul. 2016) 6173–6191, https://doi.org/10.1007/s10853-016-9909-4.

[44] Y. Ping, R.J. Kirkpatrick, P. Brent, P.F. McMillan, X. Cong, Structure of calcium silicate hydrate (C-S-H): near-, mid-, and far-infrared spectroscopy, J. Am. Ceram. Soc. 82 (3) (1999) 742–748, https://doi.org/10.1111/j.1151-2916.1999.tb01826.x.

[45] M.I. Haque, I.B. Borno, R.I. Khan, W. Ashraf, Reducing carbonation degradation and enhancing elastic properties of calcium silicate hydrates using biomimetic molecules, Cem. Concr. Compos. 136 (Feb) (2023), https://doi.org/10.1016/j.cemconcomp.2022.104888.

[46] N.Y. Mostafa, A.A. Shaltout, H. Omar, S.A. Abo-El-Enein, Hydrothermal synthesis and characterization of aluminium and sulfate substituted 1.1 nm tobermorites, J. Alloys Compd. 467 (1–2) (Jan. 2009) 332–337, https://doi.org/10.1016/j.jallcom.2007.11.130.

[47] R.I. Khan, W. Ashraf, J. Olek, Amino acids as performance-controlling additives in carbonation-activated cementitious materials, Cement Concr. Res. 147 (Sep) (2021), https://doi.org/10.1016/j.cemconres.2021.106501.

[48] Flemming A. Andersen, Ljerka Brečević, Infrared spectra of amorphous and crystalline calcium carbonate, Acta Chem. Scand. 45 (1991) 1018–1024.

[49] C. K. Huanc and P. F. Konn, "INFRARED STUDY OF THE CARBONATE MINERALS," Miiler and Wilkins. [Online]. Available: http://pubs.geosciencewo rld.org/msa/ammin/article-pdf/45/3-4/311/4252838/am-1960-311.pdf.

[50] S.-D. Wang, K.L. Scrivener, HYDRATION PRODUCTS OF ALKALI ACTIVATED SLAG CEMENT, 1995.

[51] V. Charitha, G. Athira, A. Bahurudeen, S. Shekhar, Carbonation of alkali activated binders and comparison with the performance of ordinary Portland cement and blended cement binders, J. Build. Eng. 53 (Aug) (2022), https://doi.org/10.1016/j.jobe.2022.104513.

[52] L. Alarcon-Ruiz, G. Platret, E. Massieu, A. Ehrlacher, The use of thermal analysis in assessing the effect of temperature on a cement paste, Cement Concr. Res. 35 (3) (Mar. 2005) 609–613, https://doi.org/10.1016/j.cemconres.2004.06.015.

[53] M. León, E. Díaz, S. Bennici, A. Vega, S. Ordóñez, A. Auroux, Adsorption of CO2 on hydrotalcite-derived mixed oxides: sorption mechanisms and consequences for adsorption irreversibility, Ind. Eng. Chem. Res. 49 (8) (Apr. 2010) 3663–3671, https://doi.org/10.1021/ie902072a.

[54] S.M. Park, J.G. Jang, H.K. Lee, Unlocking the role of MgO in the carbonation of alkali-activated slag cement, Inorg. Chem. Front. 5 (7) (Jul. 2018) 1661–1670, https://doi.org/10.1039/c7qi00754j.

[55] Z. Zhang, G.W. Scherer, Measuring chemical shrinkage of ordinary Portland cement pastes with high water-to-cement ratios by adding cellulose nanofibrils, Cem. Concr. Compos. 111 (Aug) (2020), https://doi.org/10.1016/j.cemconcomp.2020.103625.

[56] M. Ben Haha, G. Le Saout, F. Winnefeld, B. Lothenbach, Influence of activator type on hydration kinetics, hydrate assemblage and microstructural development of alkali activated blast-furnace slags, Cement Concr. Res. 41 (3) (Mar. 2011) 301–310, https://doi.org/10.1016/j.cemconres.2010.11.016.

[57] E. Dubina, L. Korat, L. Black, J. Strupi-Šuput, J. Plank, Influence of water vapour and carbon dioxide on free lime during storage at 80 C, studied by Raman spectroscopy, Spectrochim. Acta Mol. Biomol. Spectrosc. 111 (Jul. 2013) 299–303, https://doi.org/10.1016/j.saa.2013.04.033.

[58] A. Sarkar, S. Mahapatra, Synthesis of all crystalline phases of anhydrous calcium carbonate, Cryst. Growth Des. 10 (5) (May 2010) 2129–2135, https://doi.org/10.1021/cg9012813.